ELSEVIER

Contents lists available at ScienceDirect

Chemical Engineering Journal

journal homepage: www.elsevier.com/locate/cej





Non-noble metal-based photoelectrocatalysts for green hydrogen production and water remediation[★]

Nicolás Alejandro Sacco ^a, Alexander Iguini ^b, Ilaria Gamba ^b, Fernanda Albana Marchesini ^a, Gonzalo García ^{b,*}

^a Instituto de Investigaciones en Catálisis y Petroquímica, INCAPE (UNL-CONICET), Facultad de Ingeniería Química, Santiago del Estero 2829, 3000 Santa Fe, Argentina ^b Instituto Universitario de Materiales y Nanotecnología, Departamento de Química, Universidad de La Laguna (ULL), PO Box 456, 38200 La Laguna, Santa Cruz de Tenerife, Spain

ARTICLE INFO

Keywords:
Green hydrogen production
Paracetamol
Nickel
Molybdenum
Titanium
Water remediation

ABSTRACT

This work explores the development of NiMo-based materials supported on TiO_2 for dual applications: photo-electrochemical green hydrogen production and degradation of paracetamol. Photoelectrocatalysts were synthesized by the wet impregnation method and calcined at 400 and 900 °C to assess the influence of thermal treatment on their properties. The catalyst calcined at 400 °C achieved higher hydrogen evolution efficiency, with current densities (j) over three times higher than those of the catalyst prepared at 900 °C, attributed to its larger surface area and photoelectrochemical properties. Both catalysts effectively degraded paracetamol under light irradiation. These findings demonstrate the potential of NiMo-TiO₂ as a sustainable and cost-effective alternative to noble metal catalysts, combining environmental remediation with renewable energy production.

1. Introduction

The rapid growth of industrialization and urbanization has significantly increased fossil fuel consumption, resulting in environmental challenges that threaten human health, ecosystems, and energy security [1,2]. Recent efforts have focused on developing environmentally friendly and cost-effective technologies to address these issues by removing pollutants, generating clean energy, and creating valuable products. Catalysis plays a pivotal role in reducing production costs and enhancing reaction efficiency, contributing to sustainable development [1,2].

Solar energy is a widely available and renewable resource, making it a key solution for addressing the global energy crisis [3,4]. Photocatalytic technology has gained attention for its ability to convert sunlight into storable chemical energy, particularly for hydrogen production. Hydrogen, as a clean energy carrier, generates only water as a byproduct and emits no carbon dioxide when it is used in a fuel cell to produce electricity. This makes hydrogen an environmentally friendly alternative for applications such as transportation, power generation, and portable energy storage, provided that the hydrogen itself is produced using renewable or low-carbon methods, such as water

electrolysis powered by solar or wind energy. With an energy density of 141 kJ/g, hydrogen surpasses fossil fuels like oil (46 kJ/g) and natural gas (55 kJ/g), making it a promising alternative for renewable energy [5,6]. However, current photocatalytic systems face limitations in efficiency and scalability for large-scale hydrogen production [7,8]. Photocatalysis and photoelectrocatalysis are advanced technologies that address two critical challenges: environmental remediation and clean energy production, such as green hydrogen. A major obstacle in water splitting is its high energy demand, with a thermodynamic minimum value of 1.23 V required for the oxidation of water to molecular oxygen (O₂). However, this process is further hindered by significant kinetic barriers, increasing the overall energy consumption [9,10].

An alternative approach involves oxidizing organic pollutants instead of water. These compounds often have much lower thermodynamic oxidation potentials (typically <0.3 V), making the reaction energetically more favorable [11]. This dual function not only purifies water but also reduces the energy required for hydrogen generation. The use of photosensitive materials can further enhance the efficiency by lowering the energy threshold for these reactions [12]. TiO₂ is extensively studied as a photocatalyst due to its chemical stability, nontoxicity, abundance, and cost-effectiveness. However, its large band

E-mail address: ggarcia@ull.edu.es (G. García).

https://doi.org/10.1016/j.cej.2025.162239

 $^{^{\}star}$ This article is part of a special issue entitled: 'HYCELTEC2024' published in Chemical Engineering Journal.

^{*} Corresponding author.

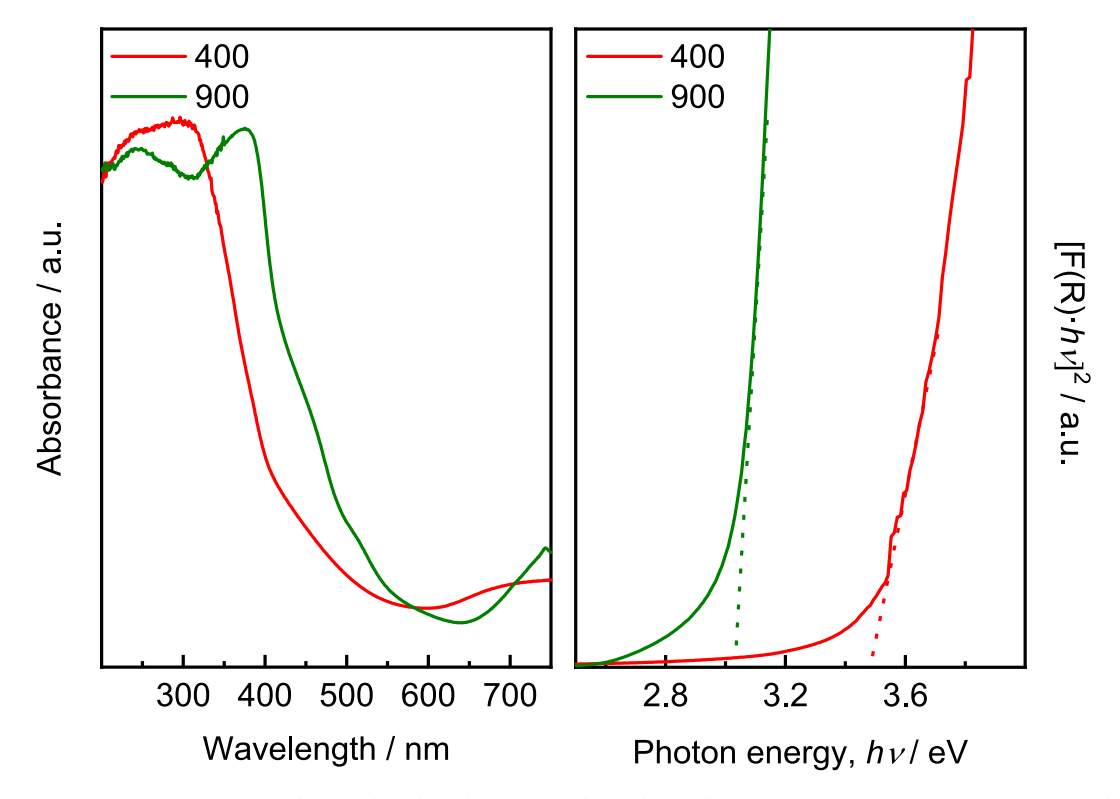


Fig. 1. UV-vis absorption spectra (left panel) and bandgap energy plot (right panel) of NiMo-TiO₂-400 and NiMo-TiO₂-900 samples.

gap (3.7 eV) restricts light absorption to the UV region, and its rapid charge recombination reduces photocatalytic efficiency [13,14]. Despite these limitations, TiO_2 remains a key material due to its suitable conduction and valence band edges, which align well with the redox potentials of water and many organic pollutants [15].

Nickel-molybdenum (NiMo) alloys have gained significant attention in the hydrogen evolution reaction (HER) at different pH conditions due to their high catalytic activity, corrosion resistance, and costeffectiveness compared to noble metals [16]. NiMo exhibits synergistic effects where Ni and Mo act as active catalytic sites for hydrogen adsorption, while Mo enhances the electronic structure, improves charge transfer efficiency, and extends light absorption into the visible region. When combined with TiO2, NiMo-based catalysts overcome the limitations of TiO2 [17] by improving electrical conductivity and introducing additional active sites for HER, making NiMo-TiO2 composites promising candidates for photocatalytic hydrogen production. In photocatalysis, a single catalyst is responsible for both pollutant degradation and hydrogen evolution. This dual role can create conflicting operational conditions, such as the need for anaerobic environments for hydrogen production versus aerobic conditions for effective pollutant oxidation [20]. Photoelectrocatalysis overcomes this limitation by using two separate electrodes, one for oxidation and another for reduction, thereby eliminating these conflicts. Additionally, simple membranes can be employed to prevent interferences, enhancing system efficiency and reliability.

Dual-functional photocatalytic systems that simultaneously produce hydrogen and degrade pollutants offer an innovative solution. These systems utilize electron reduction for hydrogen recovery and hole oxidation for pollutant degradation, addressing critical environmental challenges such as water scarcity, pollution, and global warming in a single process [18,19]. This integrated approach, particularly relevant for wastewater treatment coupled with renewable energy generation, has become a focus of growing scientific interest [20–22].

While noble metals like platinum are highly efficient for the hydrogen evolution reaction (HER), their high cost and scarcity limit practical applications [23,24]. As a result, research has shifted towards

non-noble metal catalysts, such as Ni or Mo, which exhibit HER efficiencies comparable to platinum at a lower cost [25–29].

In this work, NiMo-based catalysts supported on TiO_2 were prepared using the wet impregnation method to serve as bifunctional catalysts for the photocatalytic removal of paracetamol from water and the simultaneous production of green hydrogen. The catalysts were calcined at two different temperatures (400 °C and 900 °C) to investigate how thermal treatment affects their structural and catalytic properties. This approach enabled the evaluation of their performance in HER and pollutant degradation, focusing on the influence of morphology and surface characteristics.

Several studies have explored the oxidation of pharmaceutical pollutants, including paracetamol, using modified electrodes [30–32]. NiMo-modified electrodes have shown promising results for electrochemical oxidation due to their high catalytic activity and stability under operational conditions [33]. The oxidation of paracetamol occurs through hydroxyl radical generation and direct electron transfer mechanisms [34,35], making NiMo a suitable candidate for this application [36,37].

Paracetamol, one of the most widely used analgesics and antipyretics, was selected as a model contaminant due to its persistence in wastewater and resistance to conventional treatments. Reported concentrations of paracetamol in wastewater reach up to 1 mg/L, with 0.1–10 $\mu g/L$ observed in surface water, posing risks to aquatic ecosystems and human health due to its bioaccumulation and toxicity [38,39]. Its widespread use and incomplete removal in wastewater treatment plants make it a relevant emerging contaminant, often detected in hospital effluents and municipal water sources.

Beyond its environmental impact, paracetamol degradation can generate toxic byproducts, requiring advanced treatment methods to ensure complete mineralization. Its molecular structure allows it to interact with electrochemical and photocatalytic systems, potentially influencing charge transfer and competing with the hydrogen evolution reaction (HER) at catalytic sites.

Thus, this study bridges the gap by systematically evaluating dualfunctional photoelectrocatalysts under conflicting conditions,

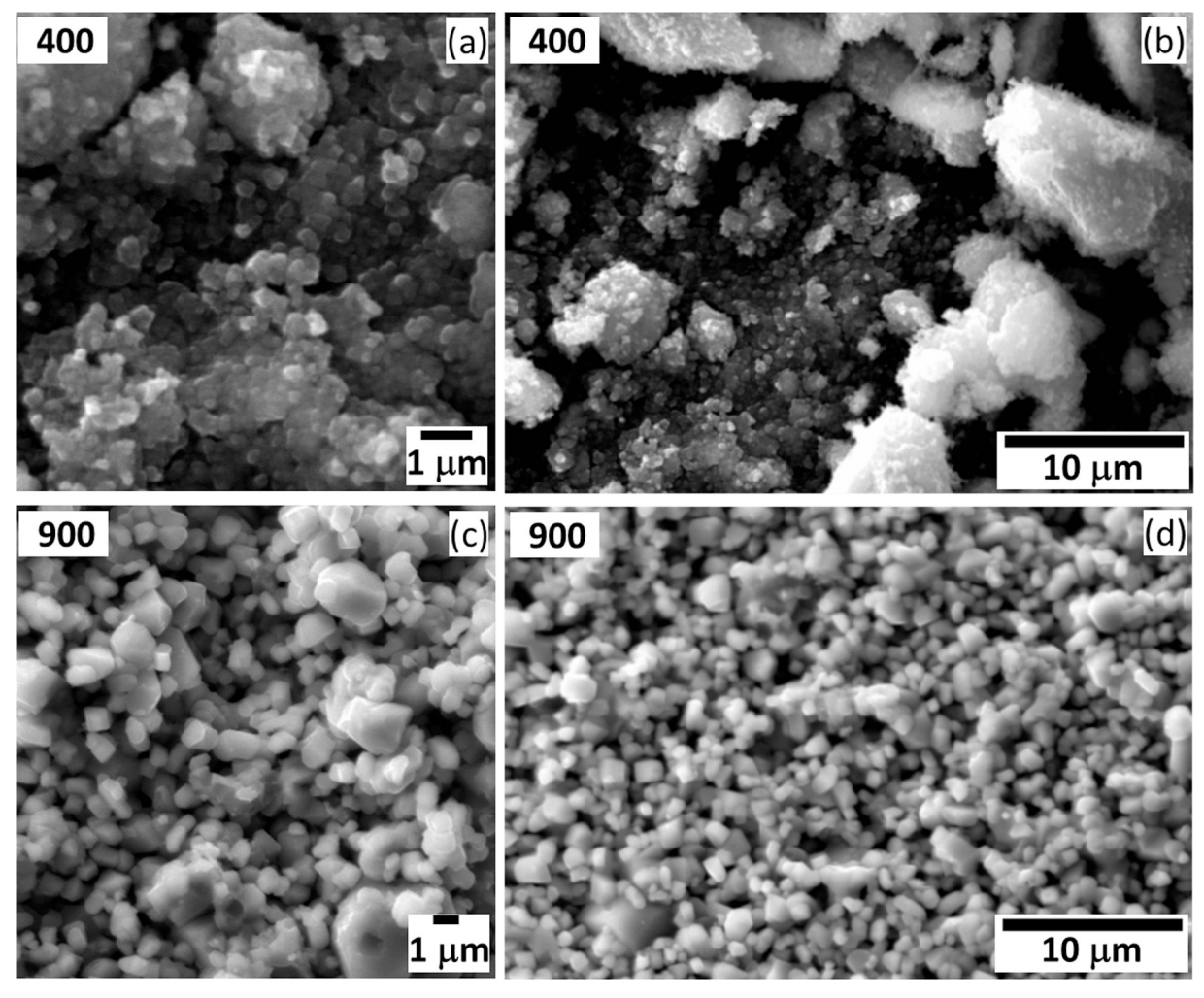


Fig. 2. SEM micrograph of catalysts calcined at 400 (top panel) and 900 °C (bottom panel).

demonstrating the feasibility of combining hydrogen evolution with pollutant degradation in a single system.

2. Experimental

NiMo-supported TiO₂ catalysts were prepared from NiCl₂6H₂O and Na₂MoO₄2H₂O precursors (Sigma Aldrich, \geq 99 %), and TiO₂ (Degussa, Zürich, Germany, P25, 48 m²/g).

2.1. Catalyst synthesis

NiMo-supported TiO₂ catalysts were prepared via the wet impregnation method. Nickel chloride hexahydrate (NiCl₂·6H₂O) and sodium molybdate dihydrate (Na₂MoO₄·2H₂O) were used as precursors. An aqueous solution containing the desired metal concentration was prepared and heated to 80 °C under stirring. The TiO₂ support was gradually added to this solution to achieve a total metal loading of 15 wt%, with a Ni:Mo molar ratio of 1.5:1. The mixture was stirred until complete solvent evaporation, followed by drying at 110 °C for 12 h. Finally, the dried powder was calcined at either 400 °C or 900 °C for 4 h in static air. The heating protocol involved a ramp rate of 1 °C/min up to 400 °C, followed by 10 °C/min for higher temperatures. The catalysts were denoted as NiMo-TiO₂-400 and NiMo-TiO₂-900. However, for simplicity, they are referred to as 400 and 900 in the figures, as only the calcination temperature was varied. This streamlined nomenclature enhances clarity and facilitates the interpretation of graphical data.

The working electrode was prepared using catalyst ink. For ink

preparation, 2 mg of catalyst powder was mixed with 15 μL of Nafion® (5 %, Sigma–Aldrich) and 500 μL of isopropyl alcohol (Sigma Aldrich, ≥ 99.7 %). The mixture was sonicated for 30 min to ensure homogeneity. A 40 μL aliquot of the ink was drop-cast onto a polished glassy carbon (GC) electrode with a diameter of 10 mm and left to dry under an inert nitrogen atmosphere. For rotating disk electrode (RDE) experiments, 12 μL of the ink was deposited onto a smaller GC electrode (3 mm diameter).

2.2. Physicochemical characterization

The crystalline phases of the catalysts were analyzed using an X'Pert PRO X-ray diffractometer (PANalytical) with $\text{CuK}\alpha$ radiation ($\lambda=1.5405~\text{Å}).$ Data was collected in the 2θ range of 20° to 100° at a scanning rate of $0.04^\circ/\text{s}.$ Phases were identified by comparing the patterns with the Joint Committee on Powder Diffraction Standards (JCPDS) database.

Morphological analysis was conducted using a ZEISS EVO 15 SEM with 2 nm resolution, coupled with an Oxford X-MAX 50 mm² energy-dispersive X-ray microanalyzer for elemental analysis. TEM analysis was performed with a JEOL JEM 2100 electron microscope at an accelerating voltage of 100 kV. The samples were dispersed in ethanol and deposited onto a standard copper TEM grid coated with a thin holey carbon film.

 N_2 adsorption–desorption isotherms were measured at $-196~^{\circ}\mathrm{C}$ using a Micromeritics ASAP 2020 system. The Brunauer-Emmett-Teller (BET) method was employed to calculate specific surface area, while

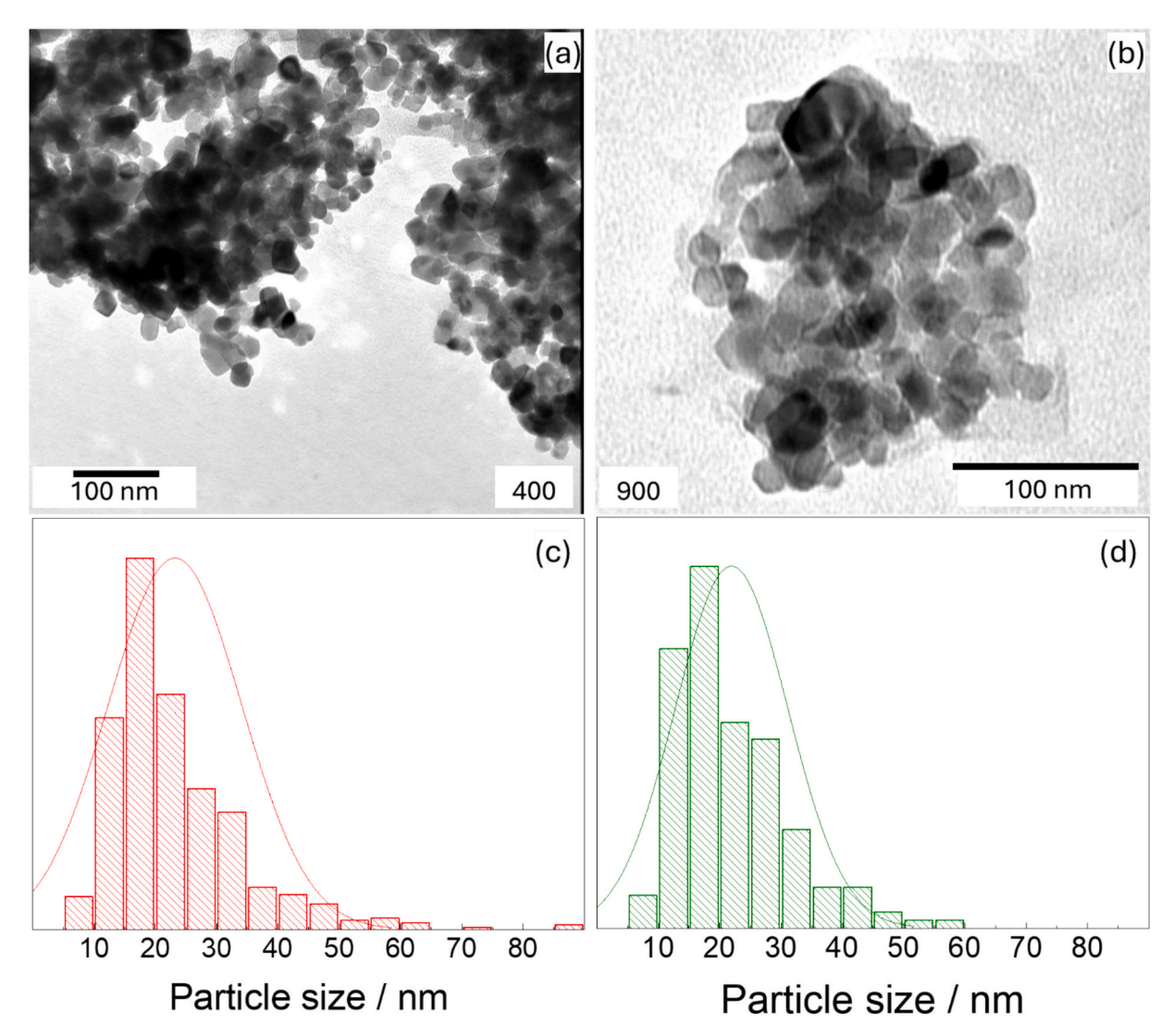


Fig. 3. HRTEM Micrographs (a and b) and Particle Size Distribution (c and d) of NiMo/TiO2 catalysts calcined at 400 and 900 °C, respectively.

pore size distribution was determined using the Barrett-Joyner-Halenda (BJH) method.

Surface chemical states were evaluated using a SPECS system with a hemispherical PHOIBOS 150 analyzer. Monochromatic AlK α X-ray radiation (200 W, 12 kV) was used, and all spectra were referenced to the C 1s peak at 284.8 eV.

Diffuse reflectance measurements were performed to determine the band-gap values of the catalysts. The band-gap values of each material were determined using the Kubelka-Munk method (K-M or F(R)), represented by Eq. (1).

$$F(R) = \frac{(1-R)^2}{2R} \tag{1}$$

In this context, R represents reflectance, and F(R) is directly related to the extinction coefficient (α). A modified Kubelka-Munk function can be derived by multiplying the F(R) function by $h\nu$, employing the relevant coefficient (n) linked to an electronic transition (refer to Eq. (2)).

$$(F(R)^*hv)^n \tag{2}$$

Plotting Eq. (2) as a function of energy in eV provides the material's band gap value. The band gap signifies the energy disparity between the valence band (the highest energy level occupied by electrons) and the conduction band (the lowest unoccupied energy level) within a material. This gap size dictates the material's capacity to absorb light and engage

in photochemical reactions. Consequently, materials with narrower band gaps typically demonstrate enhanced efficiency in utilizing a broader spectrum of light energy, necessitating less energy for electron promotion to the conduction band.

2.3. Photo/electrochemical characterization

A temperature of 20 $^{\circ}$ C was selected to evaluate the electrochemical performance of the catalysts in a three-electrode cell, controlled using a GAMRY Reference 620 Potentiostat/Galvanostat. The reference electrode used was a reversible hydrogen electrode (RHE), and all potentials mentioned below are reported relative to this electrode. The counter electrode was a glassy carbon (GC) rod, while the working electrode was prepared as an ink applied to a GC disk. Tests using a rotating disk electrode (RDE) AUTOLAB RDE-2 were conducted under the same conditions. Current density values were calculated based on the geometrical area of the working electrode.

The electrochemical behavior of the catalyst powders in a phosphate buffer solution, with and without 100 mg·L $^{-1}$ paracetamol (PTM), Sigma Aldrich, ≥ 99.9 %, purged with pure N $_2$ (99.99 %, Air Liquide) before each measurement, was investigated using cyclic voltammetry (CV) and chronoamperometry techniques. Electrolytic solutions were prepared using potassium phosphate salts (H $_2$ KPO $_4$ and HK $_2$ PO $_4$) and water (Milli-Q, Millipore) to prepare a 0.1 mol·L $^{-1}$ solution with a pH of

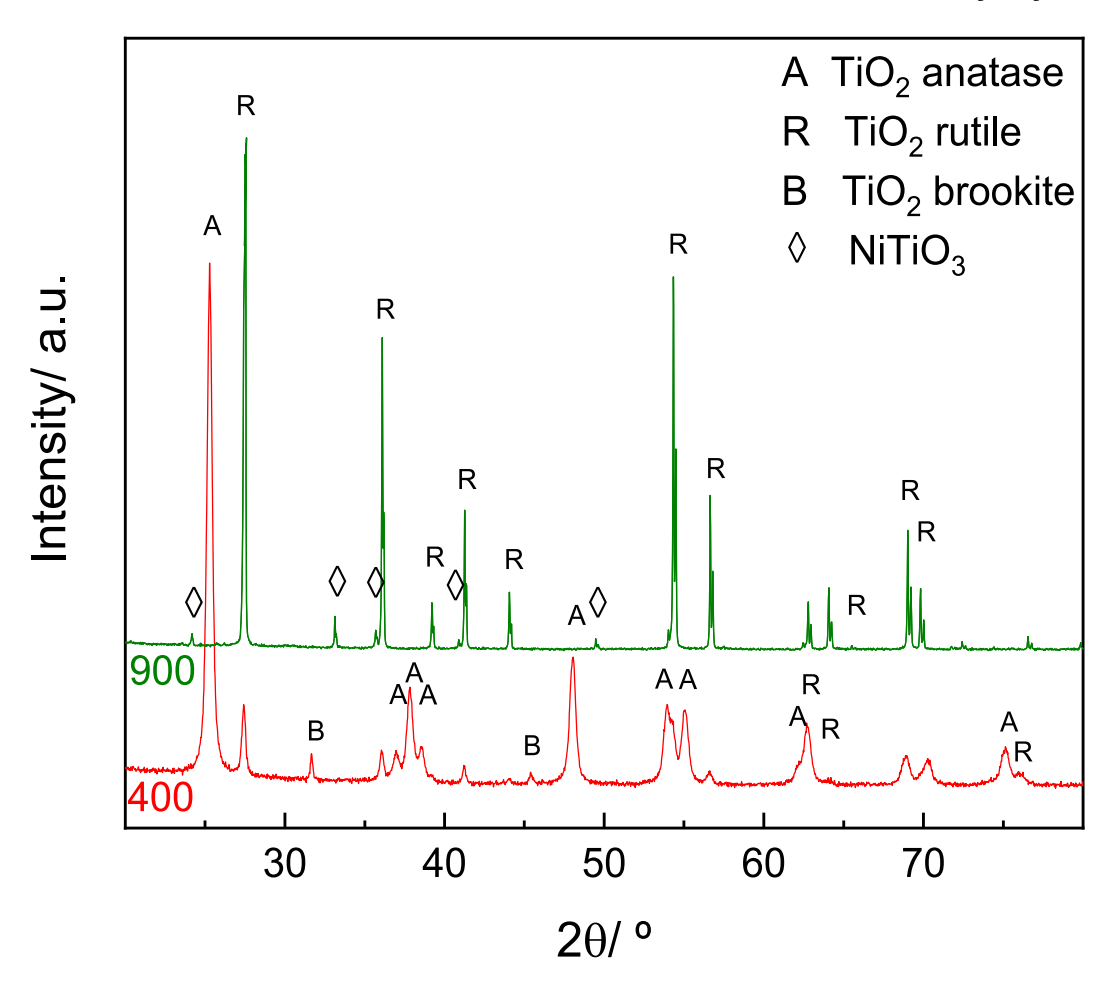


Fig. 4. XRD patterns of NiMo-TiO₂ samples calcined at 400 (red line) and 900 °C (green line). (For interpretation of the references to colour in this figure legend, the reader is referred to the web version of this article.)

Table 1Oxidation State Distribution and Binding Energy (BE/eV) of Chemical Species.

Chemical species	400		900		
	BE/eV	Atomic %	BE/eV	Atomic %	
Ni ²⁺	855.9	35.9	855.9	72.0	
Ni ³⁺	857.6	64.1	857.6	28.0	
Mo ⁴⁺	230.7	7.2	230.6	2.9	
Mo ⁶⁺	232.3	92.8	232.4	97.1	
Ti ³⁺	456.8	2.2	456.8	2.9	
Ti ⁴⁺	458.7	97.8	458.2	97.1	
O_L	529.9	62.4	529.8	58.5	
O_V	531.0	37.6	530.7	41.5	

7.

A Xe lamp XSS-5XD (Power 150 to 320 W, Radiant Output: 50 W) was used as the light source to evaluate the photoelectrochemical properties of the materials. The experiments were conducted with a light intensity of 57,500 lx (lumens/ m^2).

Photoelectrochemical properties were assessed using chronoamperometry and cyclic voltammetry (CV) techniques, both with and without irradiation. The temperature of the working solution was monitored throughout the experiments, and no variations were observed. All electrochemical experiments were conducted in the absence of oxygen. To ensure this condition, the electrolyte, both in the presence and absence of the contaminant, was deoxygenated by bubbling $\rm N_2$ with 99.999 % purity (Air Liquide) for 20 min prior to each experiment.

3. Results and discussion

3.1. Physicochemical characterization

Regarding the photochemical properties, the UV–Vis absorption spectra in Fig. 1 shows the optical properties of the catalysts calcined at 400 °C and 900 °C, respectively. For the catalyst calcined at 400 °C, the absorption edge is observed around 350–380 nm, corresponding to the bandgap transition [40]. This indicates the material's ability to absorb in the UV region, typical of TiO₂-based materials in the anatase phase. The spectrum also shows slight light absorption in the visible region, likely due to surface modifications or introduced defect states. In contrast, the catalyst calcined at 900 °C shows an absorption edge slightly shifted toward 360–400 nm, indicating the presence of the rutile phase, which absorbs at longer wavelengths due to its narrower bandgap [40,41].

The band gap was calculated using the Kubelka-Munk equation (Fig. 1), resulting in values of 3.48 eV and 3.04 eV for NiMo-TiO $_2$ -400 and NiMo-TiO $_2$ -900, respectively, smaller than the obtained for bare TiO $_2$ (3.67 eV) [42].

Morphology and elemental properties of catalysts were studied by SEM-EDS and transmission electron microscopy (TEM) techniques. Fig. 2 shows SEM micrographs of catalysts calcined at 400 (a,b) and 900 °C (c,d). The size and morphology of the particles of NiMo-TiO2 catalysts are affected by the calcination temperature. At 900 °C, the particles exhibit a more regular shape, more rounded edges, and smoother surfaces, which is closely associated with the phase transformation of the support. SEM-EDS analysis (not shown) yielded a Ni:Mo molar ratio of 1.6 ± 0.4 and 1.6 ± 0.6 for catalysts calcined at 400 and

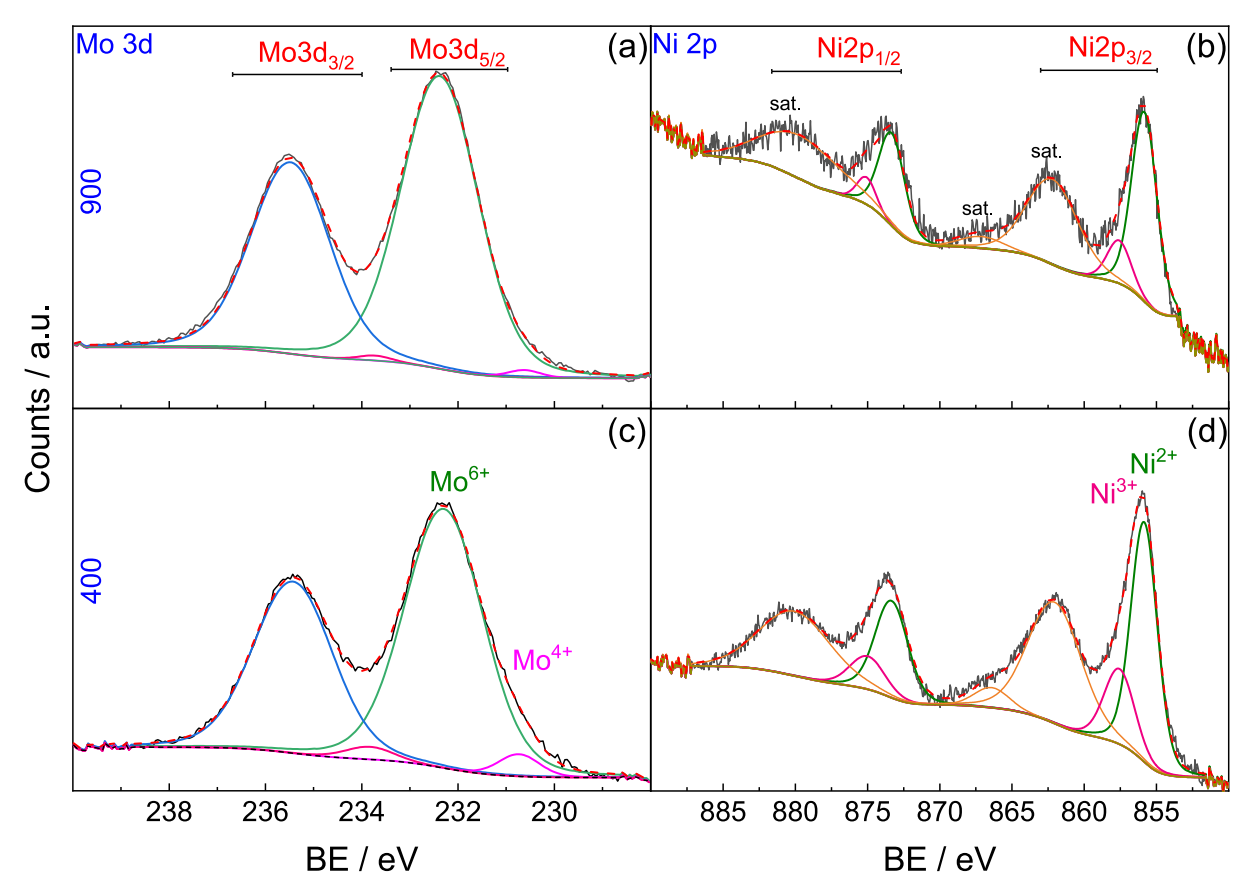


Fig. 5. XPS spectra of Mo 3d (left panel) and Ni 2p (right panel) for catalysts calcined at 400 (bottom panel) and 900 °C (top panel).

900 °C, respectively.

TEM images confirm the morphological evolution of NiMo/TiO₂ catalysts with calcination temperature (Fig. 3). At 400 °C, the particles are well-dispersed, whereas at 900 °C, significant agglomeration is observed, consistent with the SEM results showing smoother and more rounded particles at higher temperatures. Although the particle size distribution remains similar, the increased aggregation at 900 °C suggests possible sintering effects, which could lead to a reduction in the available surface area. The particle size distributions for the catalysts were estimated by counting over 200 units from different regions and HRTEM micrographs, yielding an average value of \approx 25 nm for both catalysts. On the other hand, NiMo-TiO₂-400 reveals a broad range of particle size distribution and higher particle sizes than NiMo-TiO₂-900.

Regarding the specific surface area, obtained from Nitrogen adsorption/desorption isotherms, the catalyst calcined at 400 $^{\circ}$ C showed a BET surface area of 50 m²/g, slightly higher than that of the support, TiO₂ (48.5 m²/g), while the one calcined at 900 $^{\circ}$ C yielded a value of 1.2 m²/g, which indicates significant sintering of the material.

XRD patterns of both catalysts were assayed to elucidate the crystalline phases present. Fig. 4 shows the corresponding diffractograms. Catalyst prepared at 400 °C shows characteristic peaks of TiO $_2$ in the anatase phase (20 = 25.3°, 37.8°, 48.9°, 55.1°, 62.6°) and rutile phase (20 = 27.4°, 36.1°, 41.2°, 56.3°). The presence of both phases indicates that calcination at 400 °C was not sufficient to convert all the TiO $_2$ into rutile. Additionally, the presence of the brookite phase was observed. The catalysts prepared at 900 °C only show the presence of the rutile phase, indicating that at this temperature the anatase phase completely transforms into rutile. Furthermore, calcination at 900 °C favored the interaction with the support, resulting in the formation of the mixed phase NiTiO $_3$. The absence of crystalline Ni and Mo oxide phases in the XRD patterns is likely due to their high dispersion on the TiO $_2$ support or their incorporation into the TiO $_2$ lattice, which results in their

diffraction signals being too weak or overlapping with those of the ${\rm TiO_2}$ phases. In addition, the presence of amorphous Ni and Mo oxides is not discarded.

The crystallite size for anatase, rutile, and brookite phases was calculated using the peaks at 20: $25.27^{\circ},\,27.46^{\circ},\,$ and $31.66^{\circ},\,$ respectively. The crystalline sizes for anatase, rutile, and brookite at 400 $^{\circ}C$ were 21.13 nm, 27.26 nm, and 55.05 nm, respectively, whereas the rutile size increased to 51.11 nm at 900 $^{\circ}C$.

XPS spectra were obtained to analyze the elemental composition of the samples. The surface analysis of both catalysts mainly revealed differences in the surface distribution of nickel and molybdenum species. In sample 400, the Ni content was 2.25 % and Mo was 3.21 %, whereas in sample 900, Ni was significantly lower (0.25 %) and Mo was higher (7.91 %). This lower Ni content on the surface of sample 900 is consistent with the possible formation of NiTiO₃ due to interaction with the support, as previously suggested. Table 1 presents the distribution of chemical species based on their oxidation states at 400 °C and 900 °C and the relative percentages of Ni²⁺/Ni³⁺, Mo⁴⁺/Mo⁶⁺, and Ti³⁺/Ti⁴⁺ were determined. Additionally, the contributions of lattice oxygen (O_L) and oxygen vacancies (O_V) were quantified and normalized.

The Mo 3d XPS spectra for the catalysts calcined at 900 (Fig. 5a) and 400 °C (Fig. 5c) provide insights into the chemical states of molybdenum and the impact of calcination temperature on its environment. In both cases, two main doublets are observed, corresponding to Mo $3d_{5/2}$ and Mo $3d_{3/2}$ spin–orbit components, which indicate the presence of different molybdenum oxidation states.

At 400 °C, the peaks at 232.2 and 235.4 eV correspond to $\mathrm{Mo^{6^+}}$, likely associated with $\mathrm{MoO_3}$, which is commonly formed under oxidative conditions [43]. A second set of peaks at 230.7 and 233.8 eV suggests the presence of $\mathrm{Mo^{6^+}}$ as $\mathrm{MoO_2}$. The presence of both $\mathrm{Mo^{6^+}}$ and $\mathrm{Mo^{4^+}}$ suggests a partially oxidized environment, where $\mathrm{Mo^{4^+}}$ species may be stabilized by interactions with the $\mathrm{TiO_2}$ support [44]. The

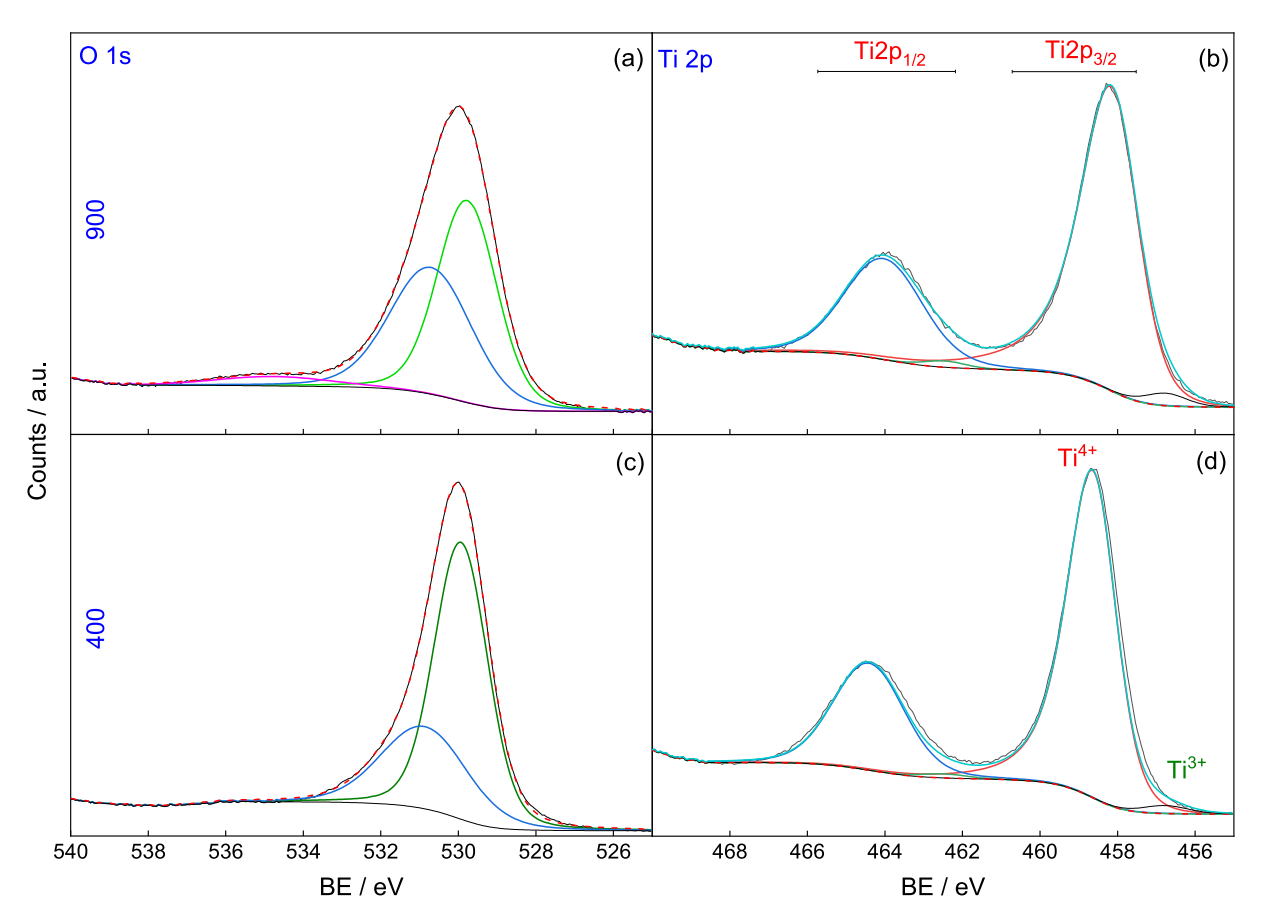


Fig. 6. XPS spectra of O 1s (left panel) and Ti 2p (right panel) for catalysts calcined at 400 (bottom panel) and 900 °C (top panel).

predominance of Mo⁶⁺ suggests that at lower calcination temperatures, molybdenum remains largely in its highest oxidation state due to the oxidative environment [45].

At 900 °C, the Mo 3d spectrum shows a shift in intensity favoring $\mathrm{Mo^{6+}}$, with peaks at similar positions (232.4 and 235.5 eV for $\mathrm{Mo^{6+}}$). The $\mathrm{Mo^{4+}}$ contribution (230.6 and 233.7 eV) diminishes significantly, indicating that the higher calcination temperature enhances the oxidation state of molybdenum [46]. This behavior is expected, as higher thermal energy promotes the complete oxidation of Mo species to $\mathrm{MoO_{3}}$, reducing the presence of partially reduced states such as $\mathrm{Mo^{4+}}$. Additionally, interactions between Mo and the $\mathrm{TiO_{2}}$ support may be altered at higher temperatures, potentially affecting the electronic properties and stability of Mo species [47].

The XPS spectra of Ni 2p (Fig. 5b and d) reveal the presence of Ni²⁺ (855.9 eV) and Ni³⁺ (857.6 eV) oxidation states, with satellite peaks indicating strong metal-support interactions.

At 400 °C, the coexistence of both oxidation states suggests the presence of mixed nickel oxides (NiO and Ni₂O₃) or highly dispersed Ni species on the TiO₂ surface. The higher proportion of Ni³⁺ at this temperature implies a partially oxidized state, which could facilitate electron transfer processes. In contrast, calcination at 900 °C leads to a relative increase in Ni²⁺ intensity, along with more pronounced satellite peaks, indicating stronger Ni-Ti interactions. These changes correlate with XRD results, which confirm the formation of NiTiO₃, where Ni is stabilized as Ni²⁺ in an octahedral coordination. This incorporation into the TiO₂ lattice reduces the fraction of Ni³⁺ observed at lower temperatures. The increased interaction with TiO₂ at 900 °C is further supported by the more intense satellite peaks, suggesting stronger electronic coupling between Ni and the support. Indeed, calcination at 900 °C favors the formation of NiTiO₃, as evidenced by the increased intensity of the peak at 855.9 eV. The transformation to NiTiO₃ reduces the number

of surface-exposed NiO species, leading to a decrease in Ni³⁺ content and enhancing structural stability at high temperatures [48].

The O 1s (Fig. 6a and b) XPS spectra reveal differences in surface oxygen chemistry between the catalysts calcined at 400 and 900 °C. Both exhibit a dominant peak at 529.9 eV and 529.8 eV, respectively, corresponding to lattice oxygen (O_L) in TiO_2 and metal oxides. Additionally, a second peak at 531.0 and 530.7 eV are present in both samples, respectively, which are attributed to oxygen vacancies (O_V) [49]. At 900 °C, the intensity of the oxygen vacancy peak increases significantly, indicating a higher concentration of oxygen-deficient sites. This suggests that thermal treatment at high temperatures enhances defect formation, likely due to the partial reduction of Ti^{4+} to Ti^{3+} , as confirmed by the Ti 2p spectra. Additionally, a more pronounced feature appears in the 533–535 eV range, attributed to adsorbed water, which is more evident in the catalysts calcined at 900 °C.

The Ti 2p spectrum of TiO₂ shows contributions from Ti⁴⁺ (458.7 eV) and Ti³⁺ (456.6 eV) [50]. A slight shift in the Ti 2p binding energy is observed, from 458.7 eV at 400 °C to 458.2 eV at 900 °C. This shift can be attributed to structural transformations, particularly the transition from the anatase to the rutile phase of TiO₂, which modifies the local lattice environment and electron density around Ti⁴⁺ ions. Additionally, the increased formation of oxygen vacancies contributes to Ti³⁺ stabilization (457 eV in Ti 2p), further modifying the electronic structure. In this context, stronger metal-support interactions between Ni, Mo, and TiO₂ at higher temperatures may also play a role in modifying the electronic states of Ti.

Accordingly, the rise of the thermal temperature induces a charge transfer from molybdenum to titanium and nickel species.

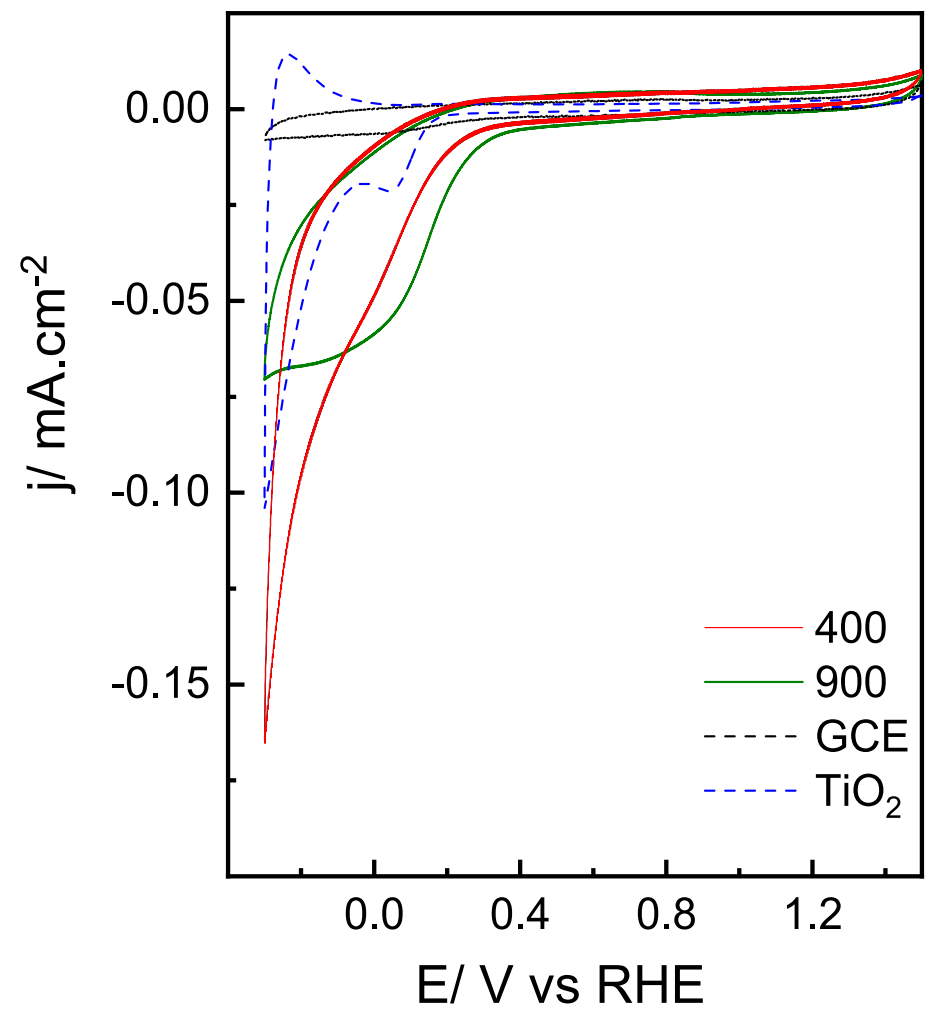


Fig. 7. Cyclic voltammograms performed at GCE (dash black line), TiO_2 (dash blue line), and $NiMo-TiO_2$ calcined at 900 °C (green line) and 400 °C (red line) in 0.1 M phosphate buffer solution, pH = 7. Sweep rate = 20 mV·s⁻¹. (For interpretation of the references to colour in this figure legend, the reader is referred to the web version of this article.)

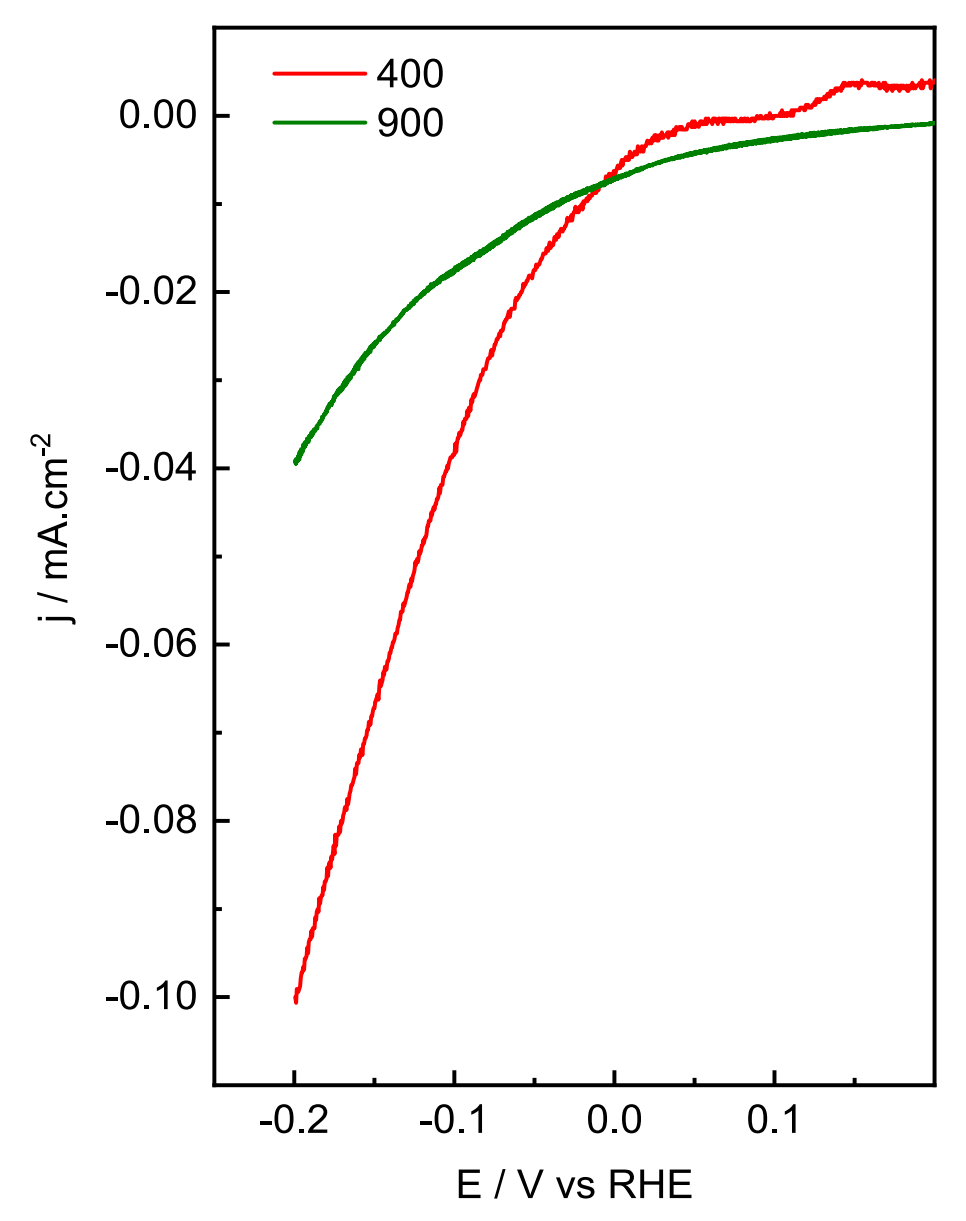


Fig. 8. Linear sweep voltammetry performed at NiMo-TiO₂ calcined at 900 °C (green line) and 400 °C (red line) in 0.1 M phosphate buffer solution, pH = 7. Sweep rate = 5 mV·s⁻¹. (For interpretation of the references to colour in this figure legend, the reader is referred to the web version of this article.)

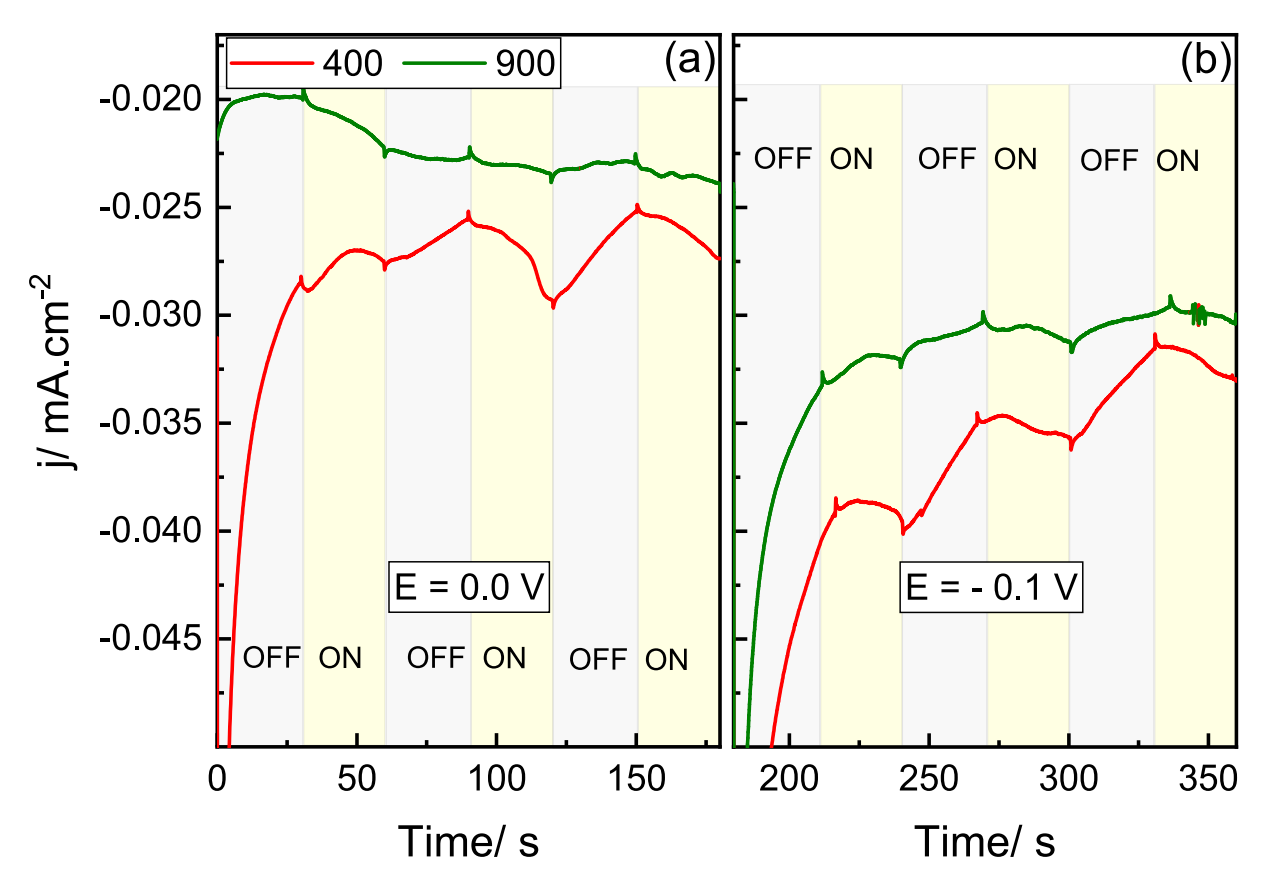


Fig. 9. Current transients of NiMo-TiO $_2$ -400 (red line) and NiMo-TiO $_2$ -900 (green line) recorded at (a) 0.0 V and (b) -0.1 V in 0.1 M phosphate buffer solution (pH = 7). The measurements were performed without electrode rotation and under an inert atmosphere. The gray-shaded regions indicate the absence of light, while the yellow-shaded regions correspond to illuminated periods. (For interpretation of the references to colour in this figure legend, the reader is referred to the web version of this article.)

3.2. Electrochemical characterization

3.2.1. Hydrogen evolution reaction (HER)

The performance of the catalysts in the HER was studied in the presence and absence of the contaminant and irradiation, through different electrochemical tests. Fig. 7 shows cyclic voltammograms performed at GCE, TiO $_2$ and NiMo-TiO $_2$ calcined at 900 and 400 $^{\circ}\text{C}$ between -0.1 V and 1.5 V in the electrolyte solution at 20 mV·s $^{-1}$.

As anticipated, the GCE electrode shows only capacitive currents within the potential range studied. On the other hand, $\rm TiO_2$ -based catalysts exhibit an increase in cathodic currents at potentials more negative than 0.40 V. Indeed, NiMo-TiO_2 calcined at 900 and 400 $^{\circ}\rm C$ reveal an increase of the cathodic current at more negative potential than 0.40 and 0.35 V, which should be associated to the electrochemical reduction of surface oxide species. Furthermore, the high increment of the cathodic current at potential more negative than 0.0 V at $\rm TiO_2$ and NiMo-TiO_2 calcined at 400 $^{\circ}\rm C$ seems to be related to the HER.

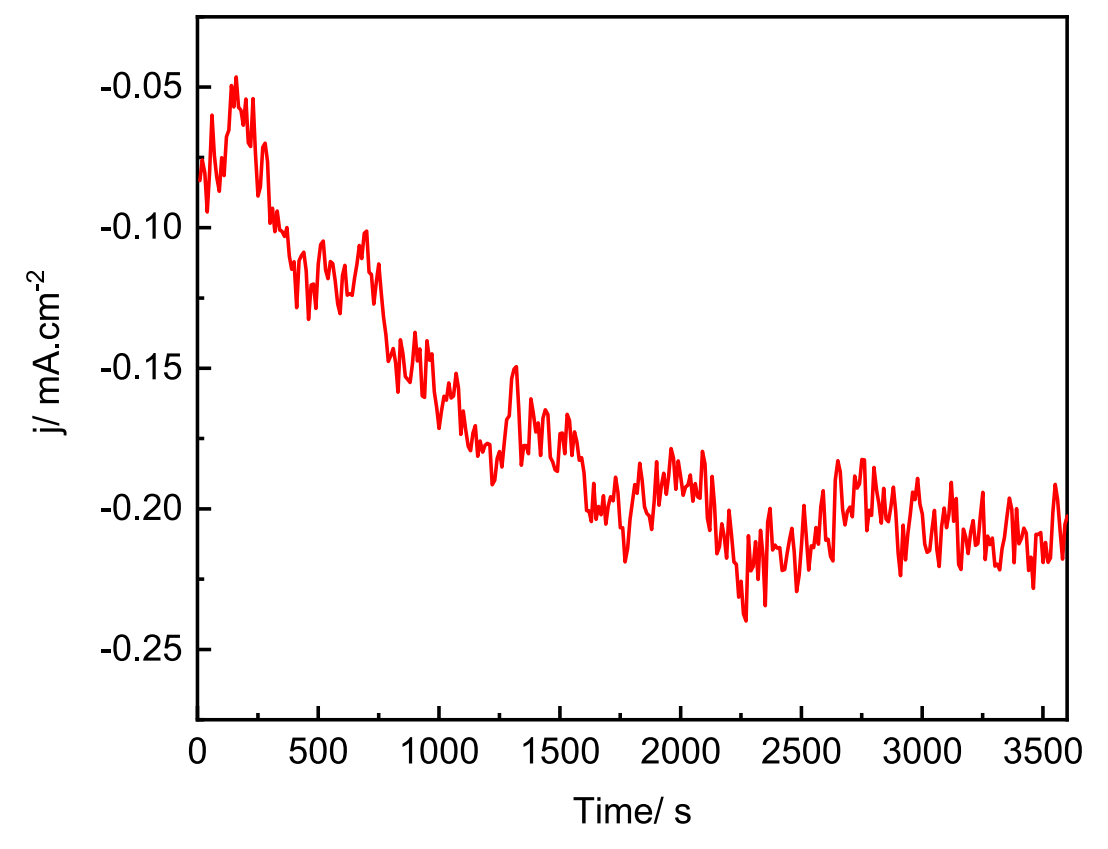
Fig. 8 shows linear sweep voltammetry (LSV) experiments for NiMo-TiO $_2$ calcined at 400 and 900 °C performed at 5 mV s $^{-1}$ to discern between faradaic currents associated to the electrochemical reduction of surface oxide species and the HER. In this context, it becomes clear the greater catalytic activity toward the HER of NiMo-TiO $_2$ calcined at 400 °C in contrast to the treated at 900 °C. Indeed, more than double current is achieved at -0.2 V with the material heated up to 400 °C in comparison with that calcined at 900 °C.

The photoelectrocatalytic performance of catalysts toward the HER was evaluated using the chronoamperometry technique. This was done in the presence (light on) and absence of radiation at 0 and -0.1 V, with a 30 s irradiation intermittence (Fig. 9). The catalyst prepared by calcination at 400 °C exhibits significantly higher cathodic current and photoactivity than that calcined at 900 °C, as the increase in cathodic current when exposed to light is much greater. This difference can be attributed to the anatase–rutile heterojunctions present in the NiMo-TiO₂-400 (band gap 3.48 eV), which enhance charge separation and reduce recombination. In contrast, the NiMo-TiO₂-900 (pure rutile, band gap 3.04 eV) exhibits faster recombination, limiting its photocatalytic efficiency. These results highlight the synergistic effect of mixed anatase–rutile phases in improving photoelectrocatalytic performance [51].

The observed current spike toward less negative current values upon illumination in both materials suggests p-type semiconductor behavior [52]. Such behavior may be associated with the presence of surface species that enhance charge transfer, underscoring the significance of calcination temperature in modulating the electronic and photoelectrochemical properties of the material [53].

On the other hand, a faster catalytic deactivation upon switch off the light at NiMo-TiO₂-400 in comparison to that heated up to 900 $^{\circ}$ C is observed (Fig. 9). This effect is more pronounced at those experiments performed at -0.1 V. These observations suggest that Mo₂O₄ is the responsible for the enhanced photoelectroactivity.

Current transient recorded at -0.1 V in the presence of light were



 $\textbf{Fig. 10.} \ \ \text{Current transient of NiMo-TiO}_2\text{-}400 \ \text{recorded at} \ -0.1 \ \text{V in 0.1 M phosphate buffer solution at rotation rate of 1000 rpm, pH} = 7, \ \text{under the presence of light.}$

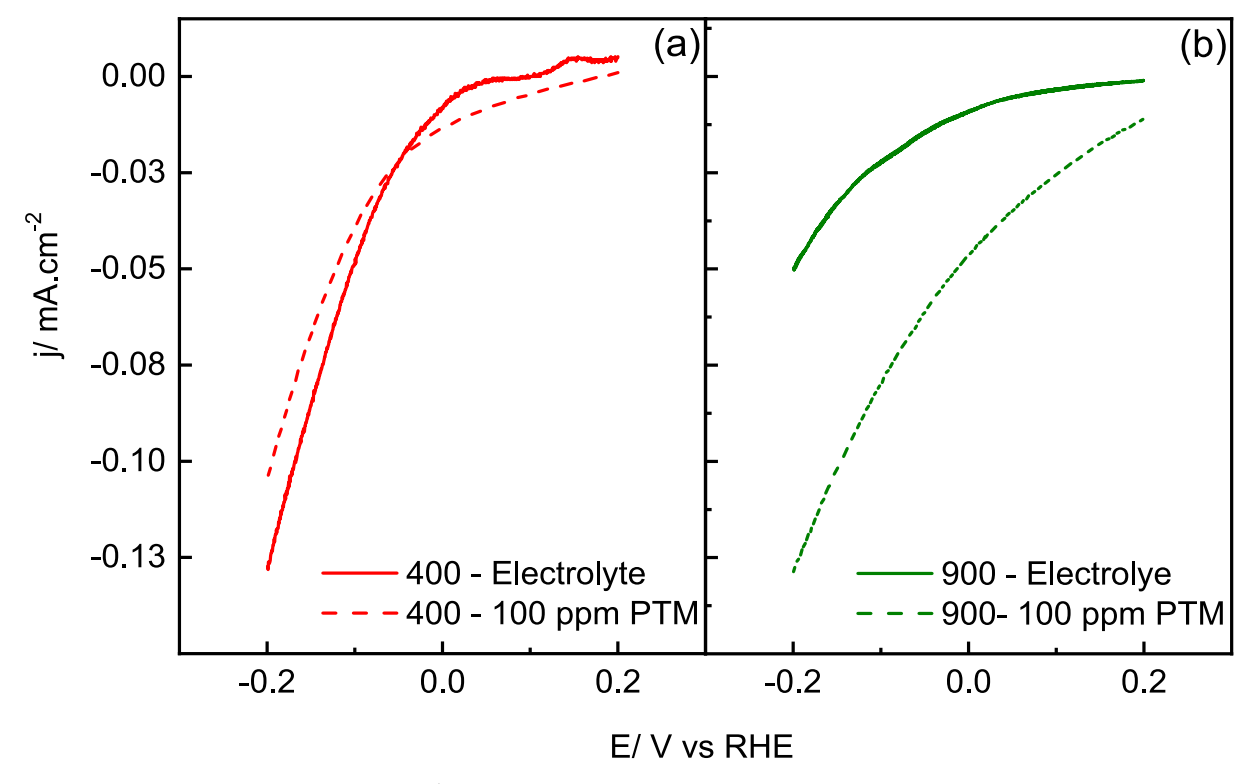


Fig. 11. Linear sweep voltammogram recorded at 5 mV·s $^{-1}$ for NiMo-TiO₂ catalysts prepared at 400 (left panel) and 900 °C (right panel) in 0.1 M phosphate buffer solution and 100 ppm of PTM solution, pH = 7.

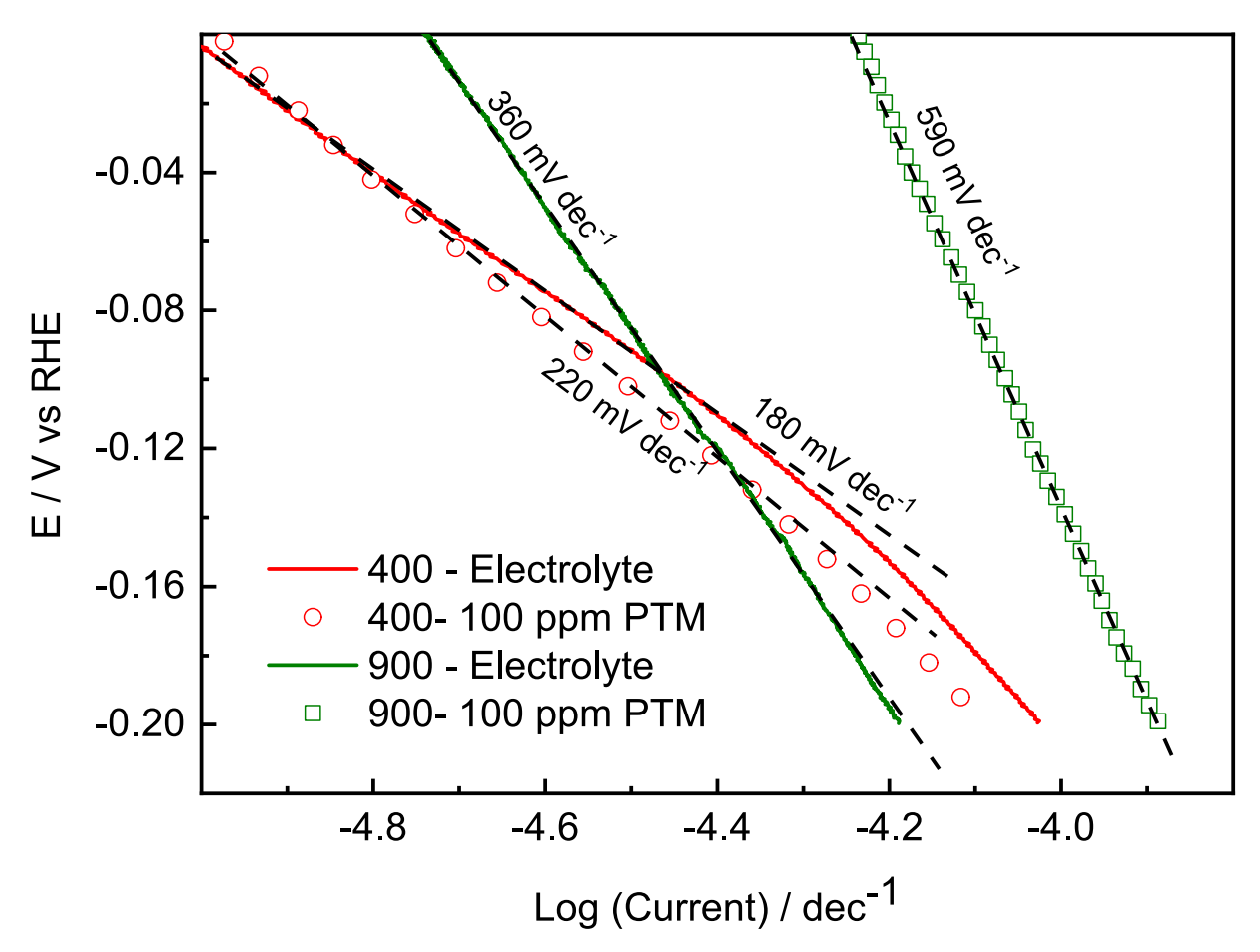


Fig. 12. Linear sweep acquired from data of Fig. 11.

performed for a long period of time at NiMo-TiO₂-400 (Fig. 10). Interestingly, the cathodic current intensely rises during the first 40 min and after that becomes constant at ca. $-0.21~\text{mA}\cdot\text{cm}^{-2}$. This behavior can be explained as the concomitant electrochemical reduction reactions of surface oxide species and hydrogen at shorter times, but the HER appears to be the only reaction occurring after 40 min of the experimental procedure. It is noteworthy that the high current noise is related to hydrogen bubbles formation and, even more importantly, the current acquired at -0.1~V in the presence of light after 40 min, which is more than 5 times higher than that developed in shorter times. Once more, Mo_2O_4 appears as the main responsible for the high photoelectrochemical activity.

Linear sweep voltammetry (LSV) was performed at both catalysts between 0.2 and -0.2 V at a sweep speed of 5 mV·s $^{-1}$ in the presence and the absence of PTM (Fig. 11). For the catalyst calcined at 400 °C, the presence of the contaminant slightly inhibits the HER. On the other hand, the catalyst prepared at 900 °C exhibited the opposite behaviour, where the current density value raises in the presence of PTM. The last indicates a surface competition between reduction of PTM and HER at NiMo-TiO₂.900, and therefore a diminution of catalytic sites for the HER is attained.

A Tafel plot was assessed to better understand the reaction kinetics and mechanism of the HER at both calcined catalysts in the absence and the presence of PTM (Fig. 12). Tafel slope (TS) values were employed to discern which reaction mechanism follows the HER at the both catalysts. In this sense, TS values of 120, 30, and $40 \text{ mV} \cdot \text{dec}^{-1}$ are associated with Volmer, Tafel, and Heyrovsky as the rate-determining step (RDS), respectively [42]:

$$Volmer: H_2O + e^- \rightleftharpoons H_{ad} + OH^-$$
 (3)

Heyrovsky:
$$H_{ad} + H_2O + e^- \rightleftharpoons H_2 + OH^-$$
 (4)

$$Tafel: H_{ad} + H_{ad} \rightleftharpoons H_2 \tag{5}$$

TS of 180 and 360 mV·dec $^{-1}$ were achieved in the absence of PTM for thermal treated catalysts at 400 and 900 °C, respectively. The elevated TS values may be attributed to the high amount of surface oxygenated species that are reduced at the same potential range that the HER occurs. Indeed, the high TS developed by catalyst calcined at 900 °C is in agreement with XPS analysis and current transients experiments, which reveal a high amount of surface oxide species. Nevertheless, both TS are attributed to the Volmer step as the RDS during the HER at the both catalysts, and the high amount of surface oxygenated species appears as the main responsible to inhibit the first electron transfer step.

The presence of PTM further influenced the TS At 400 $^{\circ}$ C due to a moderate increase from 180 to 220 mV·dec $^{-1}$ suggests competitive adsorption of PTM, partially inhibiting the HER. However, this effect was more pronounced at 900 $^{\circ}$ C, where the slope increased from 360 to 590 mV·dec $^{-1}$. These findings underline the critical role of calcination conditions in tailoring the structural and catalytic properties of the material. For dual-functional systems, such as those targeting green hydrogen production and pollutant degradation, the 400 $^{\circ}$ C-calcined catalyst emerges as a more effective and promising option, demonstrating superior electrochemical activity under both reaction conditions.

Table 2 summarizes the electrocatalytic performance of various Ni-based HER catalysts, including both NiMo/TiO₂ materials synthesized in the current study. These catalysts exhibited HER activity in neutral pH (phosphate buffer, pH = 7), achieving current densities between $-0.07-0.13 \, \text{mA} \cdot \text{cm}^{-2}$ at $-0.1 \, \text{V}$ vs RHE with a catalyst loading of 0.20

Table 2Electrocatalytic performance of different Ni-based materials for the Hydrogen Evolution Reaction (HER).

Electrode Electrocatalyst		j/mA·cm	1-2	Conditions	Ref.
Name	Load mg·cm ⁻² / (Composition)				
GCE		-0.02	Phosphate	20 mV·s ⁻¹	[42]
TiO_2	0.20/(1.25 wt%	-0.1	buffer	$E=-0.3\;V$	
PdIn/	PdIn)	-0.22	solution	vs RHE	
TiO ₂		-0.08	0.1 M (pH = 7)	5 mV·s ⁻¹ E = -0.2 V vs RHE	
GCE		-0.005		100 ppm	
TiO ₂	0.20/(1.25 wt%	-0.1		PTM	
PdIn/	PdIn)	-0.3		$20 \text{ mV} \cdot \text{s}^{-1}$	
TiO ₂				E = -0.3 V vs RHE	
NiMo/	0.20	-0.13		$5 \text{ mV} \cdot \text{s}^{-1}$	This
TiO ₂ -	(15 wt% NiMo)			$E=-0.1\;V$	work
400				vs RHE	
NiMo/		-0.07			
TiO ₂ -					
900					
NiMo/		-0.11		100 ppm	
TiO ₂ -				PTM ,	
400				5 mV⋅s ⁻¹	
NiMo/		-0.13		$E=-0.1\;V$	
TiO ₂ -				vs RHE	
900	1 41 /	15	0 F M II CO	гv1	FE 43
NiO Ni/TiO	1.41/ (≈38 wt% Ni)	−15 −50	0.5 M H ₂ SO ₄ , 5 mV·s ⁻¹		[54]
Ni/TiO ₂ Ni-NiO/	(~30 WL% INI)	-50 -70	(pH = 0.03) E = -0.5 V	e DUE	
TiO ₂		-/0	L = -0.3 V	10 IUIE	
SL Ni	0.0013Pt	≈-6	H ₂ saturated	KOH 0.1 M, 50	[55]
(OH) ₂ -	0.001311 0.0013 Ni	0	mV·s ⁻¹	1.011 0.1 111, 00	[00]
Pt/C			E = -0.2 V	vs RHE	
ML Ni		≈-5	_ 0.2 •		
(OH) ₂ -		-			
Pt/C					

mg·cm $^{-2}$ and 15 wt% NiMo. These values are comparable to PdIn/TiO₂ [42], which reached $-0.08~\text{mA}\cdot\text{cm}^{-2}$ at -0.2~V vs RHE, suggesting that NiMo/TiO₂ exhibits competitive activity at less negative potentials.

The Ni/TiO₂ catalyst (38 wt% Ni, 1.41 mg·cm $^{-2}$) reported by Gomaa et al. [54] demonstrated significantly higher current densities ($-50 \text{ mA}\cdot\text{cm}^{-2}$ at -0.5 V, pH 0.03), which can be attributed to the higher overpotential applied and the higher Ni content, as well as to the electrolyte (acidic media). Despite containing a lower active phase concentration, NiMo/TiO₂ remains active under neutral conditions, where HER kinetics are inherently less favorable.

A broader perspective on Ni-based HER catalysts can be gained by analyzing the NiMo/C (MOF-derived) system reported by Senthil Raja et al. [16], which exhibited overpotentials of 22 mV (alkaline), 48 mV (acidic), and 98 mV (neutral) at 10 mA·cm $^{-2}$. The enhanced performance of this system is associated with a higher catalyst loading (0.5 mg·cm $^{-2}$), carbon encapsulation, and the use of a Ni mesh support, which contributes to improved charge transfer and additional HER-active sites. In contrast, NiMo/TiO₂ is supported on TiO₂, an electrically insulating material, which may limit its conductivity but enhances chemical stability and absorbs UV light. Despite these differences, NiMo/TiO₂ demonstrates notable HER activity in neutral conditions, reinforcing its potential for applications where electrochemical stability and scalable fabrication methods are of essential considerations.

HER studies on Ni(OH)₂-Pt/C catalysts (Chi et al., [55]) further illustrate the importance of optimized active phase dispersion rather than just catalyst loading. At -0.2 V vs RHE, a 50 wt% Ni(OH)₂-Pt/C catalyst achieved \sim 5.2 mA·cm⁻² (multilayer) and \sim 5.8 mA·cm⁻² (single-layer), despite a significantly lower total catalyst loading (0.00226 mg·cm⁻²). These results highlight the relevance of interfacial

engineering strategies in enhancing HER activity, which could be further explored to optimize NiMo/ ${\rm TiO_2}$ -based systems.

Additionally, studies on Ni-based 3D-printed electrodes [56] reported notable HER activity in 1 M KOH, achieving 10 mA·cm $^{-2}$ at overpotentials of 337–367 mV. However, these materials required higher catalyst loadings (0.133–0.178 g·cm $^{-2}$). Although HER kinetics are inherently more favorable in alkaline conditions, the performance of NiMo/TiO $_{\!2}$ in neutral pH remains competitive despite operating under less favorable conditions.

The results highlight the potential of NiMo/ TiO_2 as a stable and scalable HER catalyst for neutral media applications. The combination of a simple wet impregnation synthesis, moderate catalyst loading, and electrochemical stability positions it as an attractive alternative for environments where strongly acidic or alkaline conditions are not viable. Further optimization of active phase dispersion, catalyst loading, and electrode interactions could enhance its efficiency while maintaining the advantages of cost-effective and large-scale production.

3.2.2. Paracetamol oxidation reaction

Fig. 13 shows cyclic voltammogram profiles of PTM electrooxidation at glassy carbon electrode (GCE, dash black line), TiO₂ (dash blue line), and catalysts prepared at 400 °C (red line) and 900 °C (green line). The oxidation of PTM on GCE generates an anodic current with a peak at 1.1 V and an onset potential of 1.0 V. The process is quasireversible, exhibiting a peak-to-peak separation of 250 mV. The catalyst prepared at 400 °C exhibited a similar behavior, with a peak separation of 330 mV, indicating greater system irreversibility. At potential more positive than the anodic peak, a significant decrease in current density is observed, exhibiting Cottrell behavior. This indicates that the process is limited by the diffusion of species toward the electrode surface. TiO2 and catalyst prepared at 900 °C show an irreversible behavior in the presence of PTM, smaller anodic current during the PTM oxidation, and at more positive potentials than the anodic peak, the oxidation behaviour differs of that developed by GCE and catalyst prepared at 400 °C. This suggests that the reaction mechanism is limited by adsorbed species at TiO2 and NiMo-TiO2-900 electrodes.

To better understand the kinetics and reaction mechanism of PTM oxidation, rotating disk experiments were conducted at various rotation rates. Besides, experiments at different sweep rates were conducted. Figs. 14 and 15 show the CV curves of PTM oxidation performed at different sweep and rotation rates, respectively.

For both studies, the evolution of the anodic currents generated by the oxidation of PTM as a function of scan rates strongly depends on the calcination temperature. An increase in anodic current was observed for both catalysts with the rise of the sweep rate, though less pronounced for the catalyst prepared at 900 °C, which did not show a Cottrell behaviour after reaching the maximum anodic current, unlike that prepared at 400 °C (Fig. 14). This suggests surface inhibition by adsorbed species.

On the other hand, when the rotation rate was varied, the anodic current related to PTM oxidation was not greatly affected for the catalysts prepared at 900 °C, while for that prepared at 400 °C, it increased with the rise in rotation rate and a diffusion-controlled reaction was discerned (Fig. 15). Additionally, both catalysts develop an increment of the anodic current in the presence of light, which reveal the great photosensibility of both materials. However, the photoelectrochemical behaviour depends of the calcination temperature. In other words, the catalyst prepared at 400 °C depicts an increment of the current in presence of light. On the other hand, an important catalytic enhancement of the PTM oxidation occurs at the material calcined at 900 °C under radiation. The last may be associated with the photoelectroxidation of adsorbed poisoning species in the presence of light.

Koutecky–Levich plots for the electrochemical oxidation of PTM on NiMo-TiO₂-400 in the presence and the absence of light are shown in Fig. 16. Employing the Koutecky-Levich equation (Eq. (6)), where I_{DIF} is the limiting current (A), I_K is the kinetic current, and I_{lev} is expressed according to Eq. (7):

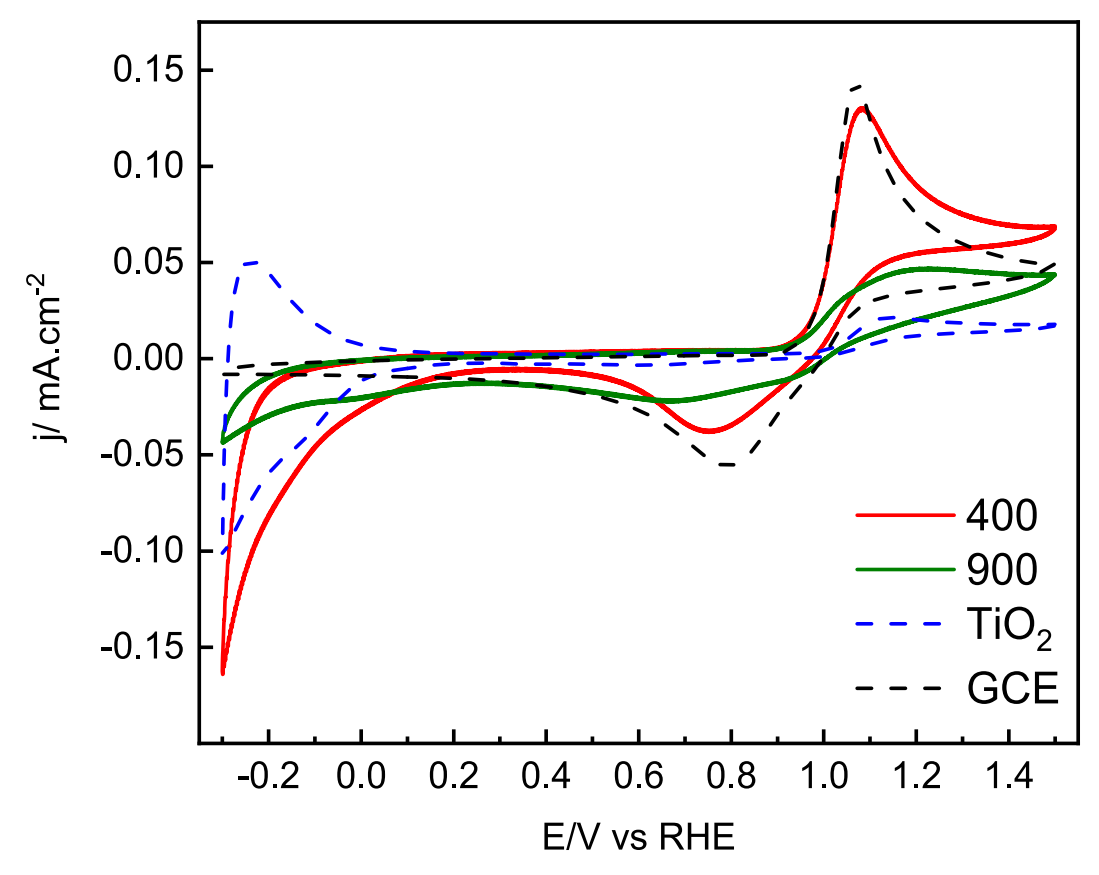


Fig. 13. Cyclic voltammograms performed at GCE (dash black line), TiO_2 (dash blue line), and $NiMo-TiO_2$ calcined at 900 °C (green line) and 400 °C (red line) in 100 ppm PTM + 0.1 M phosphate buffer solution, pH = 7. Sweep rate = 20 mV·s⁻¹. (For interpretation of the references to colour in this figure legend, the reader is referred to the web version of this article.)

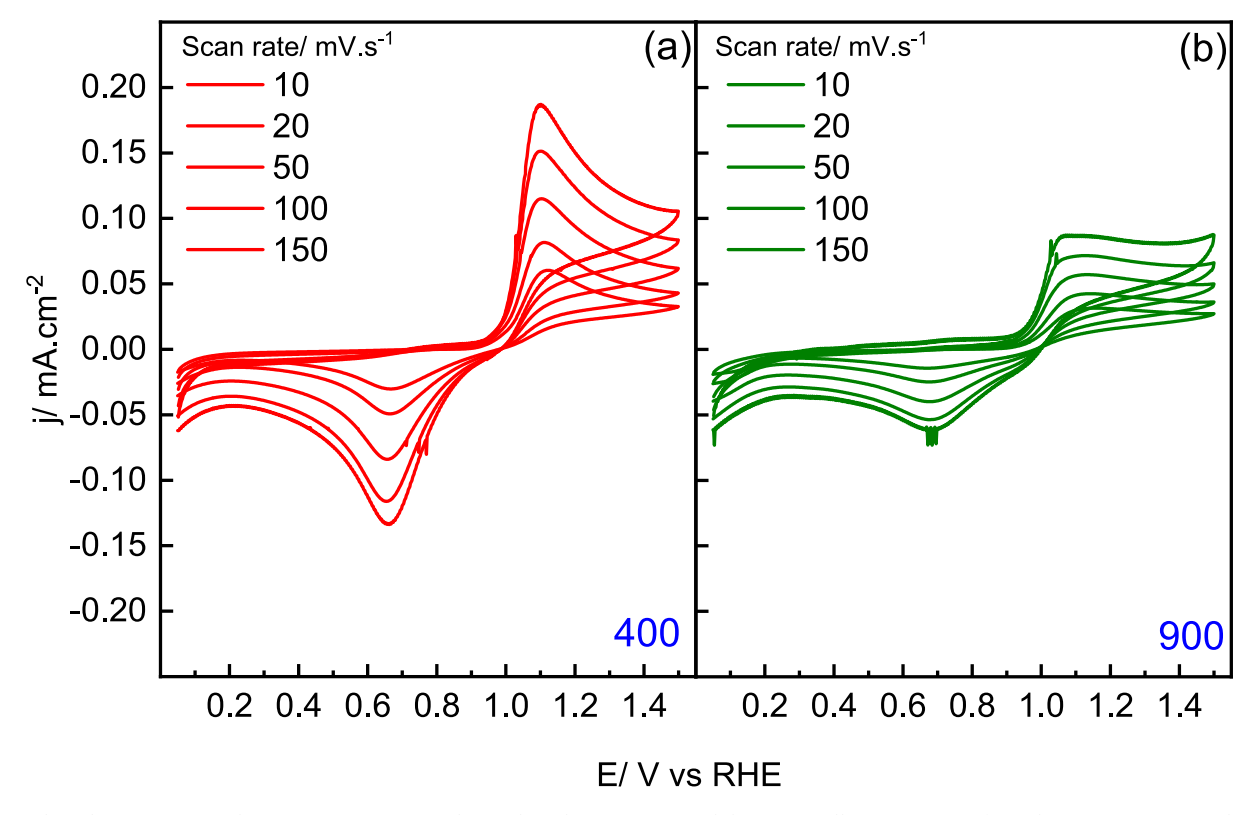


Fig. 14. Cyclic voltammograms at diverse sweep rates at catalysts calcined at (a) 400 $^{\circ}$ C and (b) 900 $^{\circ}$ C. All assays were performed in a 100 ppm PTM solution +0.1 M phosphate buffer, pH =7.

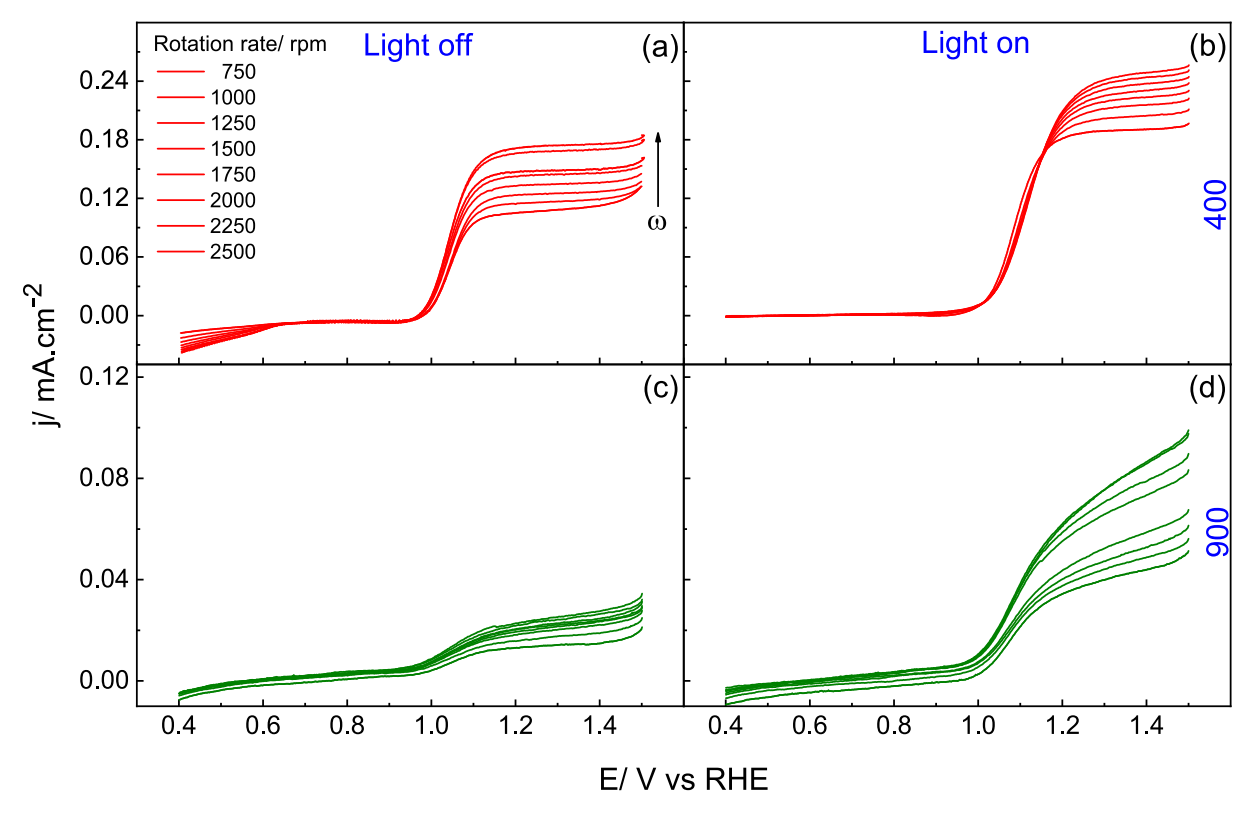


Fig. 15. Steady-state polarization curves for catalysts calcined at 400 °C (top panel) and 900 °C (bottom panel) recorded at 10 mV·s⁻¹ at several rotation rates in the presence (right panel) and in the absence (left panel) of irradiation. All assays were performed in a 100 ppm PTM solution +0.1 M phosphate buffer, pH = 7.

$$\frac{1}{I_{DIF}} = \frac{1}{I_{lev}} + \frac{1}{I_{K}} \tag{6}$$

$$I_{lev} = 0.62nFAD^{2/3}\omega^{1/2}v^{-1/6}C \tag{7}$$

where v is the kinematic viscosity, w is the angular frequency of rotation (rad·s⁻¹), A is the disk electrode area (cm²), and other symbols have their conventional meanings.

their conventional meanings. By plotting $1/I_{DIF}$ vs $\omega^{-1/2}$ and employing the kinematic viscosity of the electrolyte (0.012 cm²·s⁻¹) and the diffusion coefficient D (6.1 × 10^{-6} cm²·s⁻¹), the number of electrons transferred involved in the oxidation of PTM is n = 1 for the reaction in the absence of light and n = 2 in the presence of light. Therefore, for NiMo-TiO₂-400 electrode, reactions (8) and (9) [57] are the most plausible to occur in the absence of light, while reactions (8)–(11) [57] are the most probable to happen in the presence of light:

$$C_8H_9NO_2 \rightleftharpoons (C_8H_8NO_2)_{ads} + H^+ + e^-$$
 (8)

$$(C_8H_8NO_2)_{ads} = C_8H_8NO_2 \tag{9}$$

$$(C_8H_8NO_2)_{ads} \rightleftharpoons (C_8H_7NO_2)_{ads} + H^+ + e^-$$
 (10)

$$(C_8H_7NO_2)_{ads} \rightleftharpoons C_8H_7NO_2 \tag{11}$$

On the other hand, NiMo-TiO₂-900 catalyst reveals an irreversible behavior and inhibition of the PTM oxidation by adsorbed species was discerned to occur in the absence of light. Thus, the number of electrons (n) transferred to the surface of the electrode was calculated through the Laviron equation (Eq. (12)) for an irreversible process, where α is the electron-transfer coefficient (0.5), and n is the number of electrons involved in the redox process:

$$E_{pA} = RT(1 - \alpha)nFlog(\nu)$$
 (12)

The number of transferred electrons was 2, and reactions (8)-(11)

are the most plausible to occur with adsorbed $\mathrm{CH_8H_7NO_2}$ acting as poisoning species. The presence of light enhances the kinetic of reaction (11) (according to Tafel analysis) and consequently the anodic current rises

To contextualize the electrooxidation of paracetamol at NiMo/TiO $_2$, its oxidation potential was compared with values reported in the literature, all expressed in the reversible hydrogen electrode (RHE) scale at pH 7 to ensure consistency. In this study, the oxidation of paracetamol on NiMo/TiO $_2$ -400 occurs at approximately 1.1 V vs RHE, exhibiting a more irreversible electrochemical behavior compared to the glassy carbon electrode (1.0–1.1 V vs RHE, $\Delta Ep=250\,\text{mV}$). In the NiMo/TiO $_2$ -900 system, a slight shift of the anodic peak towards higher potentials is observed, suggesting that surface interactions play a significant role in the oxidation process.

When compared to other Ni-based materials, NiMo/TiO2 exhibits oxidation potentials within the expected range while offering the advantage of being a structurally stable and scalable alternative. Most studies on the electrooxidation of paracetamol focus on its detection, leading to differences in experimental conditions and performance evaluation criteria. Makhlouf et al. [58] reported a peak oxidation potential of ca. 1.4 V vs RHE for Pt-Ni/Screen Printed Electrode, achieving efficient electron transfer due to the presence of Pt. However, this system was designed for sensing applications, and the high cost and limited scalability of Pt-based materials pose challenges for broader electrochemical applications. Babulal et al. [59] investigated Fe-doped NiO, which also exhibited an onset oxidation potential of ca. 1.0 V vs RHE, emphasizing its role in paracetamol detection. Abdi et al. [60] studied NiNPs-SDS/CS, reporting a peak oxidation potential at ca. 1.1 V vs RHE, closely aligning with NiMo/TiO₂-400 (1.1 V RHE). The similarities in oxidation behavior suggest that both systems rely on Ni(III)/Ni(II) redox transitions, which are well-documented in Ni-based oxidation mechanisms. However, the NiNP-based system was also developed for sensing applications rather than bulk electrooxidation.

These comparisons indicate that NiMo/TiO2 operates within the

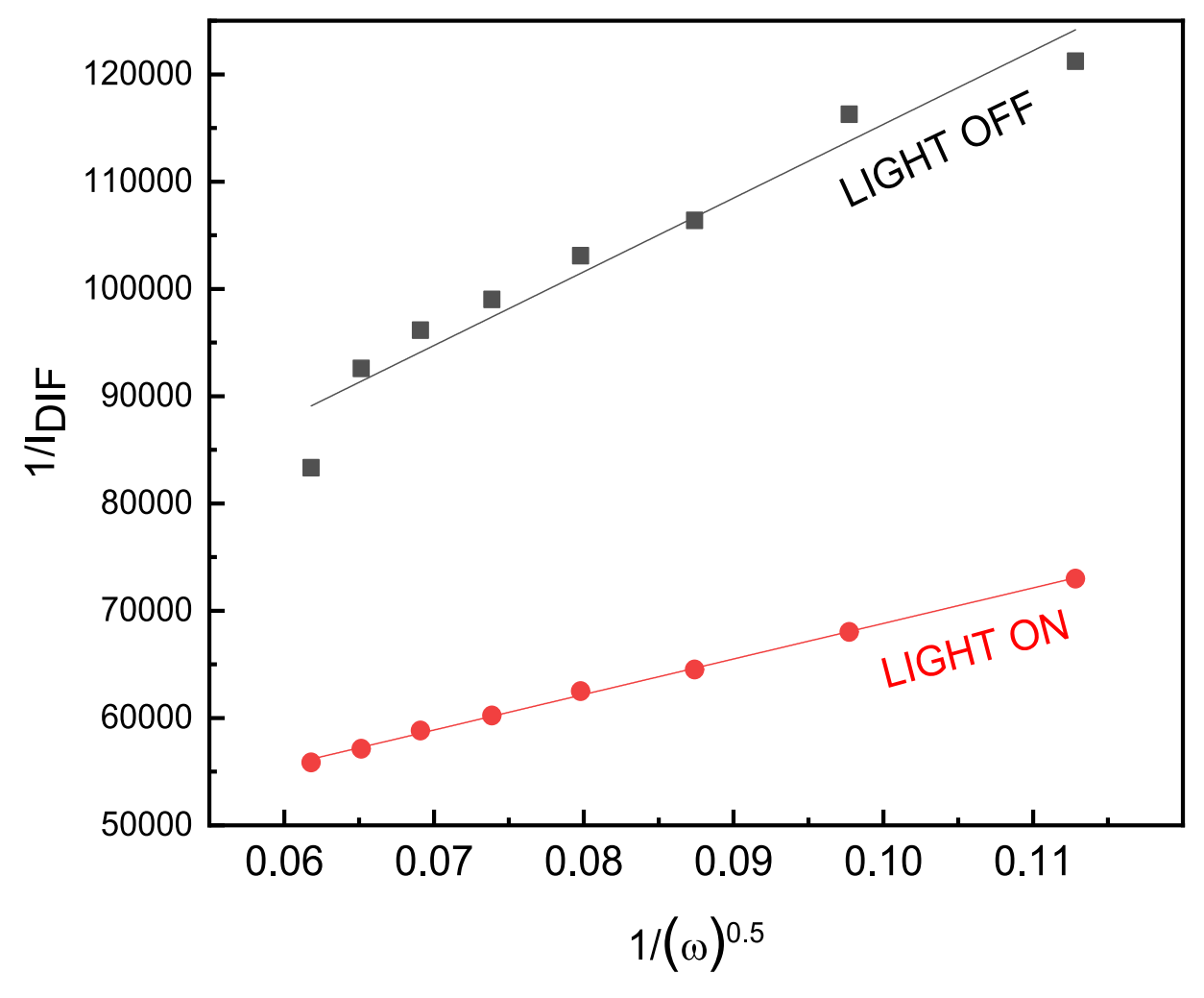


Fig. 16. Koutecky-Levich plot for oxidation of PTM at NiMo-TiO₂-400 at different rotation speeds in the presence (red circles and line) and in the absence (black squares and line) of light. (For interpretation of the references to colour in this figure legend, the reader is referred to the web version of this article.)

expected potential range for Ni-based catalysts while offering distinct advantages in terms of stability, cost-effectiveness, and fabrication scalability. Unlike Pt-containing electrodes, which present economic and material constraints.

Summarizing, NiMo/TiO $_2$ calcined at 400 °C acts as bifunctional photoelectrocatalyst. The catalyst reveals an outstanding photocatalytic performance towards the HER in neutral media, which is not compromised in the presence of PTM. On the other hand, the photoelectrochemical oxidation of PTM is not only elevated but also is limited by diffusion and therefore inhibition by adsorbed species is not perceived. Furthermore, MoO $_2$ appears as the key species to generate molecular hydrogen and degrade PTM at smaller overpotentials than the well-known water splitting. The latter is of great importance to achieve the desired hydrogen economy.

4. Conclusions

This study demonstrates the dual functionality and stability of NiMobased photocatalysts on TiO_2 for green hydrogen production and photoelectrochemical degradation of paracetamol. Catalyst calcined at 400 °C outperformed that calcined at 900 °C in HER and PTM oxidation, attributed to their higher surface area, favourable optoelectronic properties and lower amount of surface oxide species. Both catalysts successfully degraded paracetamol under light irradiation, with oxidation reaction mechanisms varying by calcination temperature. These findings underscore the potential of NiMo-TiO $_2$ as a sustainable, cost-

effective alternative to noble metal catalysts, paving the way for integrated solutions in environmental remediation and renewable energy applications.

CRediT authorship contribution statement

Nicolás Alejandro Sacco: Writing – review & editing, Writing – original draft, Methodology, Data curation. Alexander Iguini: Methodology, Data curation. Ilaria Gamba: Resources, Project administration, Conceptualization. Fernanda Albana Marchesini: Supervision, Conceptualization. Gonzalo García: Writing – review & editing, Writing – original draft, Supervision, Resources, Project administration, Funding acquisition, Formal analysis, Conceptualization.

Declaration of competing interest

The authors declare that they have no known competing financial interests or personal relationships that could have appeared to influence the work reported in this paper.

Acknowledgments

The authors thank MCIN/AEI/10.13039/501100011033 (PDI2020-117586RB-100), CECE, ACIISI (PROID2024010029 and PROID2024010032), for funding and SEGAI-ULL for collaboration. Ministry of Science, Technology, and Innovation (MINCyT) for the

granted "Academic and Professional Training Internships abroad for Argentines"; NANOtec, INTech, and Cabildo de Tenerife for laboratory facilities.

Data availability

Data will be made available on request.

References

- M. Zybert, Applied catalysis in chemical industry: synthesis, catalyst design, and evaluation, Catalysts 13 (2023) 607, https://doi.org/10.3390/catal13030607.
- [2] R. Xu, Z. Xue, S. Yang, J. Xu, H. Nie, Q.-L. Yan, Enhancing the reaction efficiency and ignition performance of core-shell Al@HMX composites by precise catalysis of graphene-based carbohydrazide complexes, Fuel 347 (2023) 128442, https://doi. org/10.1016/j.fuel.2023.128442.
- [3] C.M.S. Kumar, S. Singh, M.K. Gupta, Y.M. Nimdeo, R. Raushan, A.V. Deorankar, T. M.A. Kumar, P.K. Rout, C.S. Chanotiya, V.D. Pakhale, et al., Solar energy: a promising renewable source for meeting energy demand in Indian agriculture applications, Sustain. Energy Technol. Assess. 55 (2023) 102905, https://doi.org/10.1016/j.seta.2022.102905.
- [4] M. Jasim Hasan AlTimimi, Solar energy. Quantum Dots Recent Advances, New Perspectives and Contemporary Applications, IntechOpen, 2023.
- [5] A. Puga, Photocatalytic hydrogen production in the context of sustainable energy, in: Photocatalytic Hydrogen Production for Sustainable Energy, Wiley, 2023, nn. 1–18
- [6] M. Zhao, The current status of hydrogen energy industry and application of hydrogen fuel cell vehicles, Highlights Sci. Eng. Technol. 59 (2023) 97–102, https://doi.org/10.54097/hset.v59i.10066.
- [7] P. MeghaSen, Enhancing efficiency of the ternary tri-chalcogenide MnPSe3 towards hydrogen evolution reaction by activating its basal plane, Int. J. Hydrogen Energy 48 (2023) 21778–21787, https://doi.org/10.1016/j.ijhydene.2023.03.044.
- [8] L. Zhong, B. Mao, M. Liu, M. Liu, Y. Sun, Y.-T. Song, Z.-M. Zhang, T.-B. Lu, Construction of hierarchical photocatalysts by growing znin2s4 nanosheets on Prussian blue analogue-derived bimetallic sulfides for solar co-production of H2 and organic chemicals, J. Energy Chem. 54 (2021) 386–394, https://doi.org/ 10.1016/j.jechem.2020.06.001.
- [9] M. Saeed, U. Shahzad, H.M. Marwani, A.M. Asiri, S. ur Rehman, R.H. Althomali, M. M. Rahman, Recent advancements on sustainable electrochemical water splitting hydrogen energy applications based on nanoscale transition metal oxide (TMO) substrates, Chem. Asian J. 19 (2024), https://doi.org/10.1002/asia.202301107.
- [10] X. Wan, G. Zhu, Z. Zhou, X. Guan, Recent progress on molecular catalysts integrated photoelectrochemical systems for water oxidation, Mater. Today Catal. 4 (2024) 100042, https://doi.org/10.1016/j.mtcata.2024.100042.
- [11] Y. Wu, T. Sakurai, T. Adachi, Q. Wang, Alternatives to water oxidation in the photocatalytic water splitting reaction for solar hydrogen production, Nanoscale 15 (2023) 6521–6535, https://doi.org/10.1039/D3NR00260H.
- [12] X. Zhang, Z. Cheng, C. Bo, Y. Sun, L. Piao, The photocatalytic wastewater hydrogen production process with superior performance to the overall water splitting, J. Colloid Interface Sci. 677 (2025) 189–197, https://doi.org/10.1016/j. jcis.2024.06.039.
- [13] W. Fu, M. Yu, M. Yang, H. Yu, Y. Yang, S. Qian, X. Dong, L. Xia, Preparation of pumice stone morphology AgAlO 2 @ZnO S-type heterojunction photocatalyst with the synergistic effect of photocatalytic degradation and hydrogen production, Cryst. Growth Des. 23 (2023) 2331–2342, https://doi.org/10.1021/acs. ced.2c01339.
- [14] Q. Wang, Y. Zhao, Z. Zhang, S. Liao, Y. Deng, X. Wang, Q. Ye, K. Wang, Hydrothermal preparation of Sn3O4/TiO2 nanotube arrays as effective photocatalysts for boosting photocatalytic dye degradation and hydrogen production, Ceram. Int. 49 (2023) 5977–5985, https://doi.org/10.1016/j. ceramint.2022.11.113.
- [15] O. Al-Madanat, Y. AlSalka, W. Ramadan, D.W. Bahnemann, TiO2 photocatalysis for the transformation of aromatic water pollutants into fuels, Catalysts 11 (2021) 317, https://doi.org/10.3390/catal11030317.
- [16] D. Senthil Raja, C.-C. Cheng, Y.-C. Ting, S.-Y. Lu, NiMo-MOF-derived carbon-armored Ni₄ Mo alloy of an interwoven nanosheet structure as an outstanding PH-universal catalyst for hydrogen evolution reaction at high current densities, ACS Appl. Mater. Interfaces 15 (2023) 20130–20140, https://doi.org/10.1021/acsami.3c01061.
- [17] S. Sarfraz, N. Khan, M. Zahra, K.H. Shah, M. Javed, A. Zidan, A. Bahadur, S. Iqbal, S. Mahmood, A. Farouk, et al., Toward efficient hydrogen generation using nickelmolybdenum catalyst and its environmental sustainability, Microsc. Res. Tech. (2024), https://doi.org/10.1002/jemt.24762.
- [18] C. Bie, L. Wang, J. Yu, Challenges for photocatalytic overall water splitting, Chem. 8 (2022) 1567–1574, https://doi.org/10.1016/j.chempr.2022.04.013.
- [19] R. Kaushik, S. Gandhi, A. Halder, Photoelectrochemical degradation of organic pollutants coupled with molecular hydrogen generation using Bi₂O₃/TiO₂ nanoparticle arrays, ACS Appl. Nano Mater. 6 (2023) 4297–4308, https://doi.org/ 10.1021/acsanm.2c05406.
- [20] K. Mishra, N. Devi, S.S. Siwal, V.K. Gupta, V.K. Thakur, Hybrid semiconductor photocatalyst nanomaterials for energy and environmental applications: fundamentals, designing, and prospects, Adv. Sustain. Syst. 7 (2023), https://doi. org/10.1002/adsu.202300095.

- [21] T. Zhang, P. Wang, Y. Li, Y. Bao, T.-T. Lim, S. Zhan, Advances in dual-functional photocatalysis for simultaneous reduction of hexavalent chromium and oxidation of organics in wastewater, Environ. Funct. Mater. 2 (2023) 1–12, https://doi.org/ 10.1016/j.efmat.2023.05.001.
- [22] N. Goodarzi, Z. Ashrafi-Peyman, E. Khani, A.Z. Moshfegh, Recent progress on semiconductor heterogeneous photocatalysts in clean energy production and environmental remediation, Catalysts 13 (2023) 1102, https://doi.org/10.3390/ catal13071102.
- [23] A.Q. Mir, S. Das, S. Rai, N.A. Shah, P. Majumder, A. Dutta, Crafting fast and efficient H₂ evolution electrocatalysts with tactical inclusion of nucleobases, ACS Catal. 13 (2023) 8238–8246, https://doi.org/10.1021/acscatal.3c01384.
- [24] T. Jella, R. Arukula, Recent progress on metal catalysts for electrochemical hydrogen evolution, in: Materials for Hydrogen Production, Conversion, and Storage, Wiley, 2023, pp. 147–180.
- [25] A. Sahasrabudhe, H. Dixit, R. Majee, S. Bhattacharyya, Value added transformation of ubiquitous substrates into highly efficient and flexible electrodes for water splitting, Nat. Commun. 2018 (2014) 9, https://doi.org/10.1038/s41467-018-0438-7
- [26] L. Yu, I.K. Mishra, Y. Xie, H. Zhou, J. Sun, J. Zhou, Y. Ni, D. Luo, F. Yu, Y. Yu, et al., Ternary Ni2(1-x)Mo2xP nanowire arrays toward efficient and stable hydrogen evolution electrocatalysis under large-current-density, Nano Energy 53 (2018) 492–500, https://doi.org/10.1016/j.nanoen.2018.08.025.
- [27] F. Wang, Y. Sun, Y. He, L. Liu, J. Xu, X. Zhao, G. Yin, L. Zhang, S. Li, Q. Mao, et al., Highly Efficient and Durable MoNiNC Catalyst for Hydrogen Evolution Reaction, Nano Energy 37 (2017) 1–6, https://doi.org/10.1016/j.nanoen.2017.04.050.
- [28] Y. Zhang, B. Ouyang, J. Xu, S. Chen, R.S. Rawat, H.J. Fan, 3D porous hierarchical nickel-molybdenum nitrides synthesized by RF plasma as highly active and stable hydrogen-evolution-reaction electrocatalysts, Adv. Energy Mater. 6 (2016), https://doi.org/10.1002/aenm.201600221.
- [29] H. Niu, Q. Wang, C. Huang, M. Zhang, Y. Yan, T. Liu, W. Zhou, Noble metal-based heterogeneous catalysts for electrochemical hydrogen evolution reaction, Appl. Sci. 13 (2023) 2177, https://doi.org/10.3390/app13042177.
- [30] F. Rahimi, A. Nasiri, M. Hashemi, S. Rajabi, S. Abolghasemi, Advances in three-dimensional electrochemical degradation: a comprehensive review on pharmaceutical pollutants removal from aqueous solution, Chemosphere 362 (2024) 142620, https://doi.org/10.1016/j.chemosphere.2024.142620.
- [31] E. Makhoul, F. Tanos, R. Manouguian, M.F. Bekheet, W. Riedel, E. Petit, G. Lesage, M. Cretin, M. Boulos, D. Cornu, et al., Cobalt-substituted porous calcium copper titanate electrodes for paracetamol degradation by an electro-oxidation/peroxymonosulfate system, Appl. Surf. Sci. 669 (2024) 160430, https://doi.org/10.1016/j.apsusc.2024.160430.
- [32] A.L.A.d. Lucena, D.D. Melo, I.L.d.S. Santana, V.d.O.M. Cavalcanti, M.M.M. B. Duarte, D.C. Napoleão, Treatment of paracetamol and propranolol via anodic oxidation, electrolyte study and kinetic analysis, Revista De Gestão Social e Ambiental 18 (2024) e010555, https://doi.org/10.24857/rgsa:v18n12-196.
- [33] M. Wang, J. Li, S. Li, L. Liu, J. He, K. Li, Y. Xu, S. Zhao, W. Zhou, C. Li, et al., Process intensification enhanced continuous flow for the effective coupling of sterol electrooxidation with H2 evolution using NiMo-based electrocatalysts, Chem. Eng. Sci. 285 (2024) 119589, https://doi.org/10.1016/j.ces.2023.119589.
- [34] L. Yang, L.E. Yu, M.B. Ray, Photocatalytic oxidation of paracetamol: dominant reactants, intermediates, and reaction mechanisms, Environ. Sci. Tech. 43 (2009) 460–465, https://doi.org/10.1021/es8020099.
- [35] L. Hurtado, O. Avilés, S. Brewer, K.K. Donkor, R. Romero, R.M. Gómez-Espinosa, O. Alvarado, R. Natividad, Al/Cu-PILC as a photo-fenton catalyst: paracetamol mineralization, ACS Omega 7 (2022) 23821–23832, https://doi.org/10.1021/ acsomega.2c02508.
- [36] S. Pahra, P. Devi, Advanced electrocatalytic performance of NiMo-engineered $Ti_3C_2T_x$ MXene for sustainable hydrogen generation from wastewater, ACS Appl. Energy Mater. 7 (2024) 8669–8682, https://doi.org/10.1021/acsaem.4c01621.
- [37] M.J. Muñoz-Batista, G.R. Bertolini, C.I. Cabello, R. Luque, E. Rodríguez-Castellón, A. Kubacka, M. Fernández-García, Novel (NH4)4[NiMo6O24H6]-5H2O – TiO2 composite system: photo-oxidation of toluene under UV and sunlight-type illumination, Appl. Catal. B 238 (2018) 381–392, https://doi.org/10.1016/j. apcatb.2018.07.041.
- [38] E. Leyva, E. Moctezuma, K.M. Baines, S. Noriega, E. Zarazua, A review on chemical advanced oxidation processes for pharmaceuticals with paracetamol as a model compound. Reaction conditions, intermediates and total mechanism, Curr. Org. Chem. 22 (2018) 2–17, https://doi.org/10.2174/1385272821666171019145520.
- [39] A.Y. Tarigan, A.J. Effendi, Kinetic study of paracetamol degradation with advanced oxidation process (AOP) combination of ozone, hydrogen peroxide and ultraviolet (O3/H2O2/UV), Jurnal Multidisiplin Madani 4 (2024) 518–527, https://doi.org/ 10.55927/mudima.v4i4.8612.
- [40] F. Abu Bakar, N.S.I. Mohd Foad, Synthesis of Tio2 photocatalyst with tunable optical properties and exposed facet for textile wastewater treatment, Results Opt. 13 (2023) 100545, https://doi.org/10.1016/j.rio.2023.100545.
- [41] M. Wang, C. Li, B. Liu, W. Qin, Y. Xie, Influence of calcination temperature on photocatalyst performances of floral Bi2O3/TiO2 composite, Catalysts 12 (2022) 1635, https://doi.org/10.3390/catal12121635.
- [42] N. Sacco, A. Iguini, I. Gamba, F.A. Marchesini, G. García, Pd:In-doped TiO2 as a bifunctional catalyst for the photoelectrochemical oxidation of paracetamol and simultaneous green hydrogen production, Molecules 29 (2024) 1073, https://doi. org/10.3390/molecules29051073.
- [43] W. Gruenert, A.Y. Stakheev, R. Feldhaus, K. Anders, E.S. Shpiro, K.M. Minachev, Analysis of molybdenum(3d) XPS spectra of supported molybdenum catalysts: an alternative approach, J. Phys. Chem. 95 (1991) 1323–1328, https://doi.org/ 10.1021/j100156a054.

- [44] I.A. de Castro, R.S. Datta, J.Z. Ou, A. Castellanos-Gomez, S. Sriram, T. Daeneke, K. Kalantar-zadeh, Molybdenum oxides – from fundamentals to functionality, Adv. Mater. 29 (2017), https://doi.org/10.1002/adma.201701619.
- [45] P. Xiong, X. Gao, W. Wang, J. Zhang, F. Song, Q. Zhang, Y. Han, Y. Tan, Effect of calcination temperature on the structure and performance of molybdenum-tin catalyst for DME oxidation, J. Fuel Chem. Technol. 50 (2022) 63–71, https://doi. org/10.1016/51872-5813(21)60120-2.
- [46] P.A. Dementev, E.V. Ivanova, M.N. Lapushkin, D.A. Smirnov, S.N. Timoshnev, Electronic structure of an ultrathin molybdenum oxide film, Phys. Solid State 62 (2020) 1787–1795, https://doi.org/10.1134/S1063783420100030.
- [47] R.J. Deeth, Local density discrete variational Xα calculations on transition-metal oxycation complexes: D-d and charge-transfer spectra of molybdenyl species, J. Chem. Soc. Dalton Trans. (1991) 1895–1900, https://doi.org/10.1039/ DT9910001895.
- [48] A.M. Tarditi, N. Barroso, A.E. Galetti, L.A. Arrúa, L. Cornaglia, M.C. Abello, XPS study of the surface properties and Ni particle size determination of Ni-supported catalysts, Surf. Interface Anal. 46 (2014) 521–529, https://doi.org/10.1002/ sia_5540
- [49] S.A. Abdullah, M.Z. Sahdan, N. Nayan, Z. Embong, C.R.C. Hak, F. Adriyanto, Neutron beam interaction with rutile TiO2 single crystal (1 1 1): Raman and XPS study on Ti3+-oxygen vacancy formation, Mater. Lett. 263 (2020) 127143, https://doi.org/10.1016/j.matlet.2019.127143.
- [50] N. Kruse, S. Chenakin, XPS characterization of Au/TiO2 catalysts: binding energy assessment and irradiation effects, Appl. Catal. A 391 (2011) 367–376, https://doi. org/10.1016/j.apcata.2010.05.039.
- [51] J. Li, S. Wei, Y. Dong, Y. Zhang, L. Wang, Theoretical study on photocatalytic reduction of CO2 on anatase/rutile mixed-phase TiO2, Molecules 29 (2024) 4105, https://doi.org/10.3390/molecules29174105.
- [52] Z. Chen, T.G. Deutsch, H.N. Dinh, K. Domen, K. Emery, A.J. Forman, N. Gaillard, R. Garland, C. Heske, T.F. Jaramillo, et al., Flat-band potential techniques. (2013) 63–85.
- [53] N.G. Menon, S.S.V. Tatiparti, S. Mukherji, Effect of calcination temperature on the microstructure and electronic properties of TiO2–ZnO nanocomposites and

- implications on photocatalytic activity, Appl. Nanosci. 8 (2018) 915–930, https://doi.org/10.1007/s13204-018-0783-z.
- [54] H.E. Gomaa, H.H. El-Maghrabi, F.A. Gomaa, P. Raynaud, A.A. Nada, Unlocking high-performance hydrogen evolution: argon-induced Ni segregation in NiO/TiO2 of core/shell catalysts, Int. J. Hydrogen Energy 86 (2024) 1010–1019, https://doi. org/10.1016/j.ijhydene.2024.08.372.
- [55] L. Wang, C. Lin, D. Huang, J. Chen, L. Jiang, M. Wang, L. Chi, L. Shi, J. Jin, Optimizing the volmer step by single-layer nickel hydroxide nanosheets in hydrogen evolution reaction of platinum, ACS Catal. 5 (2015) 3801–3806, https:// doi.org/10.1021/cs501835c.
- [56] M. Khalil, I. Dincer, Experimental investigation of newly designed 3D-printed electrodes for hydrogen evolution reaction in alkaline media, Energy 304 (2024) 132017, https://doi.org/10.1016/j.energy.2024.132017.
- [57] D. Nematollahi, H. Shayani-Jam, M. Alimoradi, S. Niroomand, Electrochemical oxidation of acetaminophen in aqueous solutions: kinetic evaluation of hydrolysis, hydroxylation and dimerization processes, Electrochim. Acta 54 (2009) 7407–7415, https://doi.org/10.1016/j.electacta.2009.07.077.
- [58] F.Z. Makhlouf, M.L. Chelaghmia, R. Kihal, C.E. Banks, H. Fisli, M. Nacef, A. M. Affoune, M. Pontié, Screen-printed electrodes decorated with low content Pt–Ni microstructures for sensitive detection of Zn(II), ascorbic acid and paracetamol in pharmaceutical products and human blood samples, Microchem. J. 206 (2024), https://doi.org/10.1016/j.microc.2024.111467.
- [59] S.M. Babulal, K. Venkatesh, S.M. Chen, S.K. Ramaraj, C.C. Yang, Fe doped NiO incorporated porous carbon hybrid electrocatalyst: a state of the art analysis for the selective sensing of acetaminophen in biological and pharmaceutical samples, J. Alloy. Compd. 876 (2021), https://doi.org/10.1016/j.jallcom.2021.160215.
- [60] S. Abdi, M.L. Chelaghmia, R. Kihal, C.E. Banks, A.G.M. Ferrari, H. Fisli, M. Nacef, A.M. Affoune, M.E.H. Benhamza, Simultaneous determination of 4-aminophenol and paracetamol based on CS-Ni nanocomposite-modified screen-printed disposable electrodes, Monatsh. Chem. 154 (2023) 563–575, https://doi.org/ 10.1007/s00706-023-03062-7.